# Pre-failure suction-induced deformation to inform early warning of shallow landslides: proof of concept at slope model scale

Coppola L. [1], Reder A.[2], Tarantino A. [3], Mannara G.[4], Pagano L.[5]

[1] Lucia Coppola, Dipartimento di Ingegneria civile, edile e ambientale, Università di Napoli Federico II, Italy (lucia.coppola@◆unina.it)

[2] Alfredo Reder, REgional Model and geo-Hydrological Impacts-REMHI, Centro Euro-Mediterraneo sui Cambiamenti Climatici, Via Thomas Alva Edison s.n.c., Caserta, 81100, Italy (alfredo.reder@cmcc.it)

[3] Alessandro Tarantino, Department of Civil and Environmental Engineering, University of Strathclyde, Scotland, UK (alessandro.tarantino@strath.ac.uk, ORCID-ID 0000-0001-6690-748X)

[4] Giovani Mannara, IVM srl - Piazza Principe Umberto I, 16 - Castellammare di Stabia, Italy (mannara@ivmtech.it)

[5] Luca Pagano, Dipartimento di Ingegneria civile, edile e ambientale, Università di Napoli Federico II, Italy (lupagano@unina.it)

CORRESPONDING AUTHOR: lucia.coppola@unina.it

KEYWORDS: shallow landslides; silty volcanic soils; soil suction; tilting; slope pre-failure deformation.

## ABSTRACT

The majority of the Landslide Early Warning Systems (LEWS) currently in operation are based on the monitoring of rainfall data alone and this limits their performance due to false alarms generated by rainfall thresholds that are inevitably set conservative. The accuracy of LEWS may be significantly enhanced by monitoring soil-based variables associated with the stress-strain response of the ground. This paper investigates whether slope pre-failure deformation can be used as additional precursor of landslide initiation. This would lead to a substantial improvement of LEWS accuracy especially if pre-failure deformation is combined with suction monitoring. Tests were carried out using a small-scale physical model of a slope built with unsaturated volcanic silt subjected to artificial rainfall. A new device named tensio-inclinometer was purposely developed to monitor simultaneously suction and suction-induced deformation. It combines a conventional tensiometer and an accelerometer installed at the top of the tensiometer shaft. It is shown that pre-failure deformation detected by the tilting of the tensiometer shaft is an adequate landslide precursor and that, combined with suction, can provide soil-based thresholds for early warning systems.

# 1 INTRODUCTION

Rainfall-induced shallow landslides in coarse-grained volcanic fall deposits often evolve into debris flows causing significant damage and fatalities worldwide. Catastrophic events have been recorded in the last two decades in El Salvador, Hong-Kong, Indonesia, Italy, Japan, Mexico, Russia, Taiwan, and Venezuela (Fuchu et al. 1999; Cascini and Ferlisi, 2003; Olivares and Picarelli, 2003; Capra et al. 2003; Crosta et al. 2005; Chen et al 2006; Pagano et al.; 2010; Mizuyama and Egashira, 2010; Santo et al., 2012; Yamao et al 2015; Chávez et al. 2016; Shimizu and Ono, 2016; Perov et al., 2017; Kusumawardani et al. 2017; Zhang et al 2022). Volcanic soils are non-plastic and are characterised by high porosity maintained by the suction generated by the partially saturated state. The loss of suction due to rainwater infiltration in association with high porosity make this class of materials susceptible to generate fast-moving debris flows. Risk reduction strategy for this class of landslides is based on Landslide Early Warning Systems (LEWS) as the rapidity of the sliding mass movement demands alarms to be issued ahead of landslide initiation (UNISDR, 2006; Alfieri et al., 2012; Greco & Pagano, 2017). LEWS need to be informed by landslide precursors and the performance of LEWS depends directly on the precursor variables to be monitored and the model used to set alarm thresholds.

Rainfall is considered the primary and often the sole precursor variable in the majority of the LEWS currently in operation (e.g. Keefer et al., 1987; Ortigao and Justi, 2001; Chleborad et al., 2008; Baum et al., 2008; Baum & Godt, 2010; Pagano et al., 2010; Formetta et al., 2016; Pecoraro et al., 2019). The relatively low accuracy of LEWS informed solely by rainfall data leads to conservative alarm thresholds. These tend to generate repeated false alarms and induce the served communities to underreact to the warning thus undermining the effectiveness of the LEWS (Greco & Pagano, 2017; Intrieri et al., 2012; Sattele et al., 2015; Reder & Rianna, 2021). A well-performing LEWS should therefore achieve accuracy not only to avoid missed alarms but also to minimise false alarms.

To enhance the performance of LEWS the monitoring of soil volumetric water content (measured by dielectric-based sensors) has been included as additional precursor variable because the variation of volumetric water content is an indicator of loss of suction and, hence, shear strength (Orense et al., 2003; 2004; Baum et al., 2010; Ponziani et al., 2012; Thiebes et al., 2014; Uchimura et al., 2015; Segoni et al., 2018). However, volumetric water content is not a very suitable landslide precursor as pore-water pressures triggering slope failures are generally in the range of a few kilopascals either in the negative or positive range (Balzano et al., 2019 a,b). In this interval, volumetric water content is characterised by poor sensitivity in the negative range of pore-water pressures (the water retention curve tends to level off when approaching saturated conditions) and no sensitivity in the positive range of pore-water pressures. Overall, current LEWS lack of effective precursors to generate more accurate warnings.

This paper aims to investigate whether suction and suction-induced pre-failure deformation can be used as landslide precursors. Shallow slope failure in silty/sandy geomaterials typically occurs with a well-defined failure surface as detected ex post (Balzano et al., 2019 a,b). The onset of failure is characterised by relatively large displacements of the mass above the failure surface generated by very high shear deformations in proximity of the failure surface (shear band). This stage can be preceded by diffuse shear and compression plastic deformations above the failure surface and are referred to as 'pre-failure suction-induced deformations' in this work. The research question addressed in this paper is whether pre-failure deformation combined with suction monitoring can provide effective precursors of landslide initiation. This would potentially lead to substantial improvement of LEWS accuracy.

A slope physical model was used to test whether wetting-induced instability is preceded by substantial pre-failure deformations. The slope was reconstituted using natural volcanic soil reproducing similar porosity and slope inclination as encountered in the field (Balzano et al. 2019b) and then subjected to artificial rainfall until failure. Soil suction and slope deformation were monitored using a tensio-inclinometer purposely developed for this research and designed to be later deployed in the field to underpin real LEWS. The tests presented in the paper aim to provide a TRL3 validation ('proof of concept' according to European Commission 2017) for the use of combined measurement of suction and slope deformation to anticipate the occurrence of rainfall-induced instability. Although the experiments presented in this paper focus on volcanic soils, the results are expected to be applicable to the wider class of coarse-grained silty materials.

## 2 THE TENSIO-INCLINOMETER

### *2.1 Concept*

The tensio-inclinometer was assembled by combining i) a conventional tensiometer to measure pore-water pressure in negative and positive range and ii) an accelerometer installed to the tensiometer shaft at its top to measure its inclination as a suitable proxy measurement of landslide pre-failure deformation (Figure 1).

Pore-water pressure is a more effective precursor than volumetric water content. Silty volcanic slopes are generally cohesionless and characterised by inclinations close to the friction angle. As a result, pore-water pressures triggering slope failures are generally in the range of a few kilopascals either in the negative or positive range. Tensiometers generally show accuracy to less than 1 kPa and can measure pore-water pressure in both negative and positive range. This makes pore-water pressure measured by tensiometers a better precursor of rainfall-induced shallow landsides. It should also be noted that tensiometer maintenance (re-saturation) is not required during the wet period, i.e., the period when the tensiometer data are expected to inform the LEWS. Maintenance is not therefore a disadvantage for tensiometers compared to water content dielectric-based sensor.

The measurement of tilting as proxy variable of slope deformation was favoured over measurement of surface displacements via total station, Global Positioning System (GPS), and photogrammetric techniques as implemented in other LEWS concepts (Barla & Antolini, 2016; Zhu et al., 2017). Adverse weather conditions affect the line of sight between observer and target in total station measurements, rain can weaken the GPS signal, and reduced visibility during rain events affects the quality of photographic images.

A metal box including the accelerometer and the electronics was clamped to the tensiometer shaft via a clamping hook to be easily removed for maintenance or replacement. The metal box was designed to retrofit any commercial tensiometer once the cables from the tensiometers are connected to the chip extension via the external sockets on the metal box.

The tensio-inclinometer was designed to operate wirelessly with power supplied by a battery and Wi-Fi data transmission. The electronics required for pore-water pressure and tilting measurement, data storage and data transmission are installed on a semiconductor chip. The battery and the semiconductor chip are located in the metal box secured to the tensiometer shaft (Figure 1). The device allows wireless monitoring of two precursor variables in a single element, which is an advantage with respect to approaches based on different elements connected by cables (e.g. Yang et al., 2017). The wireless design enables rapidity of installation and/or replacement and avoids malfunctioning due to cable damage by wild animals.

## *2.2 Accelerometer and tensiometer*

The tensiometer (T4, UMS GmbH, Munich, Germany) consists of an acrylic-glass shaft of variable length in-between 0.15-2 m, developed to monitor pore-water pressure in the range from - 85 kPa to 100 kPa (Figure 1). A high air-entry value saturated ceramic cup is positioned at the bottom of the shaft to allow water (under tension) to flow from the soil to the tensiometer water reservoir or vice versa. Water pressure in the tensiometer water reservoir is measured by a piezo-electric pressure sensor positioned at the top of the tensiometer water reservoir. The back of the sensing diaphragm is vented to the atmosphere via the electrical cable and, as a result, the tensiometer measures gauge pore-water pressure. The electrical cable carrying the power supply and the output analog signal was connected to an external plug located on the metal box. The sensing diaphragm has an accuracy of better than ±0.5 kPa.

The acceleration measurement system is based on MEMS (Micro-Electro-Mechanical- Systems) capacitive accelerometer that measures the part of gravity accelerations activated by the tilting. The accelerometer returns in the three tilting components as shown in Supplementary Figure S1. An accuracy of 0.05° can be achieved for the shaft tiling angle.

## *2.3 Electronics*

### *2.3.1 Primary semiconductor chip*

An 'all-in-one' primary chip includes (1) MEMS accelerometer, (2) power supply, (3) power management, (4) data storage and (5) signal digitisation data wireless transmission (microcontroller) (Supplementary Figure S2).

Lithium Thionyl Chloride (Li-SOCl2) non-rechargeable batteries supply power to the system. Batteries can ensure an acquisition every ten minutes for more than one year and may be easily replaced once fully discharged. Each section is provided with a power management system, adjusting batteries voltage according to requirement of each component (2V for MEMS accelerometer and microcontroller digital circuits, 3.3 V for the analogic circuits, 5 V for the tensiometer digital circuit).

A highly performing microcontroller (codification CC1352R) is linked to all sensors and to the memory to manage all system components. It integrates a wireless transceiver, which ensures good transmission quality with the external receiver without suffering from significant electrical disturbance deriving from microcontroller activity.

A non-volatile memory (codification MX25R6435F) stores all device data. The memory capacity of 64 Mbit can ensure storage of data acquired every ten minutes for more than one year. The tensiometer extension of the semiconductor chip includes the 16 bit analog-to-digital converter (ADC). The 16-bit resolution allows pore-water pressure to be measured with resolution better than 0.01 kPa. The chip extension was designed for two tensiometer connections. In this way, two adjacent tensiometers of different length (installed in close proximity to each other to measure suction at two different depths) can be connected to a single metal box.

### *2.3.2 Extension semiconductor chip*

An extension of the semi-conductor chip including (6) power supply for the tensiometer pressure sensors and (7) analog-digital converter for the tensiometer output signal (Supplementary Figure S2). Data storage and transmission for the tensiometers was achieved via the same components installed on the primary board used for tiltmeter data.

### *2.3.3 Operating modes*

The prototype firmware and management software were developed to operate according to two different operation modes (Supplementary Figure S3):

- the data collection and real-time transmission (Wi-Fi) operation mode (DC);
- the data logger operation mode (DL) and bulk transmission on demand.

Once the data are acquired, DC mode performs a mere wireless real-time data-transfer of all digitised data, while DL mode operates the data storage followed by a wireless bulk data-transfer when requested remotely. The DC mode is activated during the rainy period when data need to be transmitted at the highest frequency to inform the early warning system. Real-time transmission is the most energy-demanding operation mode, and it is therefore only active during the wet period. The DL mode is activated during the dry period. Although tensiometer and inclinometer data are not critical in this period, it is assumed that it is still valuable acquiring pore-water pressure and deformation data. To save battery energy charge, data are acquired at lower sampling rate, stored on-board on non-volatile memory, and periodically transmitted in bulk on user demand.

The data acquisition cycle is shown in Supplementary Figure S3. At regular predetermined time intervals, the primary chip including the accelerometer and ADC and the chip extension connected to the tensiometers are switched on. The system remains on for 10 seconds to allow for tensiometer warm-up. The same time span is exploited by the ADC for self-calibration. On completion of the warm-up stage, the acquisition stage takes place. This is followed by DC data transmission or alternatively DL data storage possibly followed by a subsequent bulk data-transfer on demand. Each stage has its specific duration, optimised to save power consumption (see list in Supplementary Table S1).

Each tensio-inclinometer transmits the data to a collector node over Wi-Fi (either in real-time in DC mode or in bulk on-demand in DL mode). Previous studies have indicated that Wi-Fi transmission works properly during rainfall (Biansoongnern et al., 2016). The collector node is designed to transmit the data to the remote computer via wired network in order to safeguard the robustness of transmission of the data used to inform the early-warning system. To this end, the collector node includes a USB port that allows either i) direct connection to a laptop or ii) connection to the wired network via a USB-to-Ethernet adaptor.

The management software also provides a CSV file containing diagnostic information about different components (temperature and battery level). Each metal box communicates wireless with a collector node, physically linked to a PC throughout USB interface.

### *2.3.4 Battery duration and data storage*

To quantify duration of battery and data storage, the scenario shown in Figure 2a was considered. It consists of one month of extremely wet period with acquisition every 30 min with real-time data transmission (DC mode), 5 months of moderately wet period with data stored on-board every 3 hours (DL mode), and 6 months of dry period with data stored on-board every 6 hours (DL mode). Figure 2b compares the cumulated adsorbed energy charge in one year with the battery capacity. The battery is clearly designed in a very conservative fashion and can last several years before replacement. Data logged on-board should be downloaded at least once a year to avoid that memory full.

## 3 SLOPE PHYSICAL MODEL

The slope physical model consisted of a tilting tank with rectangular base 2 m long and 1.5 m wide (Figure 3). The height of the side walls allowed accommodating a soil layer with a maximum height of 0.5 m (in the direction orthogonal to the base). The slope physical model was designed to have the width-to-thickness ratio relatively high to minimise the effect of friction along the longitudinal boundaries. This was assumed to be a key aspect of the experimental design as lateral friction could hinder pre-failure deformation of the slope.

The side walls were built with a lower part made of steel ($h_1$ = 0.2 m) and an upper part made of Plexiglas® ($h_2$ = 0.3 m) to allow for lateral visual inspection of the slope. The downslope wall was made of a perforated steel sheet to maintain the soil layer in place once the tank was tilted and allow for water drainage at the same time. A geotextile was interposed between the base of the tank and the soil layer to increase the interface frictional resistance and promote the development of a failure surface well within the soil layer.

The tank base was supported by a steel frame with a hinge located at the tank mid-length. A hydraulic actuator operated manually allowed tilting the tank up to 45°. The tank was surmounted by three steel portals carrying each brass nozzles to generate nebulised rain. The nozzles have 1.19 mm wide orifice tips allowing water flow rates in the range between 0.32 to 1.95 l/min for water pressures between 0.2 and 10 bars respectively.

The tested soil was a non-plastic, cohesionless silty sand of volcanic origin (Figure 4). Drained isotropic-consolidated triaxial tests (not yet published) yielded a friction angle of $\phi'$=33°. Permeameter laboratory tests (not yet published) yielded a saturated hydraulic conductivity of $3\times10^{-7}$ m/s.

A high-resolution digital video camera was positioned normal to the soil layer surface to enable measurement of surface displacements via Particle-Image Velocimetry (PIV). The analysis has been performed using PIVlab, a free toolbox for MATLAB® (Thielicke and Stamhuis, 2014). The input images were divided into sub-images (interrogation areas), and for each of these, a cross-correlation was performed. The resulting correlation matrix is used to estimate the most probable displacement within each interrogation area. An interrogation area of 86 x 100 pixels (width and height respectively) has been used. It was therefore checked that the displacements did not change when the size of interrogation area was either increased to 151 x 206 pixels or decreased to 64 x 72 pixels.

## 4. RESULTS

Three tests have been carried out to explore the effect of soil bulk density and the role of vegetation. Test 1 was carried out on bare slope prepared with loose volcanic silt, 30 cm thick, and tilted to 36°. Tests 2 and 3 were carried out on slopes prepared with dense volcanic silt, 35 cm thick, vegetated with graminaceous plants, and tilted to 45°. The tank was initially positioned horizontally to form the soil layer by dry pluvial deposition and to allow vegetation to grow (tests 2 and 3). The tank was then tilted and an artificial rain of 28 mm/h was applied until global instability was observed.

### Test 1

Average soil porosity after placement was determined by averaging the porosity of three samples taken from the layer at different locations and found equal to 67%. After deposition, the layer was moistened by rain sprinkles and covered with a waterproof sheet to allow for hydraulic equilibration for two weeks. The tank was then tilted to an angle of 36° greater than the soil friction angle.

It is worth noticing that the 'effective' inclination of the slope is lower than the inclination of the tank. The downslope wall imposes a constraint on the kinematics of global instability and forces the failure surface that forms parallel to the base of the tank in the upper portion of the slope to flatten mid-slope to reach the rim of the downslope wall. The 'effective' inclination of the slope (overtaking angle) is approximately given by the inclination of the segment joining the bottom of the upslope wall with the top of the downslope wall. This inclination was equal to 27.5° and actually governs the global instability.

The slope was monitored by four tensio-inclinometers. These were installed slightly leaning upslope with the heavy box at the top of the shaft turned upslope. This generated a moment that slightly compressed the soil at the contact with the upslope portion of the shaft. Devices $D^1_1$, $D^1_2$ and $D^1_3$ were installed quasi-vertically with backwards angles of 1-2°. $D^1_1$ and $D^1_3$ were pushed down to the bottom of the layer while $D^1_2$ was pushed down to the layer mid-height. Device $D^1_4$ was installed with a backward angle of 10° to explore the effect of a more eccentric top box. The positions of nozzles, tensio-inclinometers, and PIV-interpreted zones are shown in Figure 5.

Rainfall initially infiltrated into the soil layer and started to run off after ~10 min from the beginning of the artificial rainfall. After 20 min, local instability phenomena were observed involving sublayers 2-3 cm thick. The global instability was observed after 80 min and took place when suction dropped to a few kilopascals.

The rapid post-failure movement observed was likely associated with liquefaction. According to Picarelli et al. (2020), liquefaction of silty volcanic soils occurs when the mobilised stress falls within an unstable zone in the mean effective stress-deviatoric stress plane that is bounded by the critical state line and a liquefaction 'instability' line. This unstable zone widens as the soil porosity increases. For the slope in question, the 'mobilised' overtaking angle (27.5°) likely fell between the critical state friction angle (33°) and the instability line pulled down by the high soil porosity.

Figure 6 shows images of the evolution over time of the test. Figure 7 shows the rotation measured by the four devices benchmarked against the surface displacement parallel to the slope at three different locations (A to C) derived from particle image velocimetry (PIV).

The devices $D^1_1$ and $D^1_3$ show rotation that increases downslope at increasing rate until global failure is reached. The measurement of the devices $D^1_1$ and $D^1_3$ is remarkably consistent and also in fair agreement with the surface displacement in the zones A and B (Figure 7a).

The measurement of device $D^1_2$ only lasted 25 min. Over this time, its measurement was also consistent with the measurements by devices $D^1_1$ and $D^1_3$. The measurement ceased after 25 min because the device $D^1_2$ experienced instability due to the attainment of limit lateral load for the shaft. The $D^1_2$ aboveground stretch was the same as $D^1_1$ and

$D^1_3$, i.e. the box at the top of the shaft generated similar torque with respect to the ground surface. However, $D^1_2$ was only inserted to the slope mid-height compared to $D^1_1$ and $D^1_3$. As a result, the pressures applied by the soil to the shaft on its downslope side were much higher to compensate for the reduced arms with respect to the ground surface. As water infiltrated into the ground and suction decreased, passive conditions were achieved and the device fell.

The device $D^1_4$ shows a progressive counter-tilting likely associated with the installation with a backward angle of 10° (Figure 7b). The portion of soil located downslope initially experienced significant surface displacement (point C in Figure 7b). The lack of support downslope to $D^1_4$ might have generated a rotational mechanism facilitating the backward rotation of the device $D^1_2$.

Figure 8 shows the simultaneous measurement of rotation and suction for the devices $D^1_1$, $D^1_2$, and $D^1_4$. A malfunctioning affected $D^1_3$, which failed in recording suction and only returned tilting evolution, and is therefore not shown in Figure 8. The device $D^1_1$ measures an initial suction of 8 kPa at the layer base. Suction progressively reduced over the test down to 2 kPa just before failure. Rotation increased consistently with suction reduction until global instability took place. It is worth noticing that the movement is recorded earlier (~20 min) than the drop in suction at ~30 min (Figure 8a). Similar observations can be made for device $D^1_2$ for the period when the shaft remained in place.

The device $D^1_4$ recorded an initial drop in suction (Figure 8b), which can partly explain the surface displacement observed at point C in Figure 7b. The rotation recorded after ~30 min, although taking place backward, also appears to be consistent with the drop in suction from 7 kPa to 2 kPa.

**Test 2**

A thicker layer (35 cm) was placed at a lower porosity and then vegetated with a grass to respectively increase the degree of particle interlocking and introduce in the layer a tightening root system.

Soil porosity after deposition was estimated by collecting three samples from the layer at different locations and measuring their porosity. It ranged between 61% and 64%. The lower porosity was expected to generate a stiffer response of the soil and, hence, probe the tensio-inclinometer to detect smaller soil deformations prior to failure.

The soil layer was sown with a mixture of twelve different graminaceous plants and repeatedly wetted over a month to facilitate vegetation growth. A single sowing was sufficient to cover the entire surface. Over this period roots reached the bottom of the tank. The tank was first tilted to 36°, the same inclination as Test 1. Three nozzles and six tensio-inclinometers were installed as shown in Figure 9. The tensio-inclinometers were pushed to the depths of 35, 25 and 10 cm (Figure 9). All the tensio-inclinometers were installed with the box at the top of the shaft turned upslope, and as close as possible to the ground surface to minimise overturning moments as observed in Test 1. The devices $D^2_{A1}$, $D^2_{B1}$ and $D^2_{C1}$ were placed in the soil quasi-vertically, the remaining devices were positioned following the direction orthogonal to the slope upper surface. The tensio-inclinometers were placed in the upper portion of the slope to minimise the effect of the kinematic constraint imposed by the downslope rigid wall. Instruments and markers were placed along three different lines labelled as A, B and C. Surface displacements were measured by a motorized total station targeting 4 markers placed at the top of shafts pushed into the soil layer and placed closed to the tensio-inclinometers of the alignment A and C.

In this first stage of the test, rainfall was applied long enough to generate slightly positive pore-water pressures. Figure 10a shows the evolution of tilting and suction measured by the $D^2_{C1}$ device (negative suction indicates positive pore-water pressure). The increase of rotation is highly consistent with the drop in suction.

A failure surface became visible upslope through the plexiglas wall (Fig.10b). A rotational movement occurred along the slip surface as indicated by the device counter tilting occurring at the end of the test (Figure 10a). However, the rotational movement stopped without generating a collapse mechanism. The mobilised 'effective' angle of 27.5° was lower than the critical state angle (33°) but also lower than the liquefaction 'instability' line pulled up by the lower porosity. As a result, neither liquefaction nor global instability took place.

Rainfall was then stopped, the slope was exposed to the atmosphere. Evapotranspirative fluxes acted for a week and suction increased again to about 4 kPa. The tank was then tilted up to 45°. This was aimed to raise the 'effective' (overtaking) inclination from 27.5° to 35°, i.e. greater than the friction angle of 33° to promote global instability of the slope.

Rainfall was applied again, with the same intensity. Rainwater initially infiltrated into the slope until some rainwater started to run-off. The presence of the diffuse root system initially inhibited local instabilities that were otherwise observed in Test 1. Global instability was observed about 70 min after the start of the rainfall. Figure 11 shows the sequence of the evolution of the slope over the test.

Figures 12, 13 and 14 show the evolution of rotation and suction recorded by the tensio-inclinometers together with the surface displacements of the markers recorded by total station. It is worth noticing that one of the tensio-inclinometer installed along the alignment B malfunctioned and data from this device are missing. As for Test 1, rotation increases as suction decreases. A rotation increase is recorded well ahead of global instability. However, the stiffer response of the soil 'reinforced' by the root system and/or the lower porosity resulted in rotations in the range 1-5° markedly lower than rotations up to 25° as recorded in Test 1 on bare soil. The evolution of rotations is highly consistent with the evolution parallel-to-slope displacements, the latter also markedly smaller than the surface displacements recorded in Test 1. Suction paths show that global instability took place under slightly positive pore-water pressures.

**Test 3**

The third test was carried out following similar deposition by pluviation as Test 2. Values of porosity after placement were consistent with those measured for Test 2. Two seeding stages were carried out to cover the entire layer surface with graminaceous plants. The first stage aimed to vegetate the central part of the surface layer whereas the second stage allowed vegetating the part of the surface layer adjacent to the walls of the tank. After about one month, the roots penetrated a relatively shallow depth (around 25 cm), i.e. roots did not reach the bottom of the tank.

The monitoring and artificial rainfall systems (Figure 15) were similar to those installed in Test 2 (Figure 9). Three different alignments considered, labelled as alignment “A”, “B”, and “C” respectively. The three nozzles used were the same of Test 2 and they were located along the alignment “B”.

Six tensio-inclinometers were installed, distributed across the three alignments (four tensio-inclinometers were placed along the alignment “A”, only one tensio-inclinometer along the remaining alignments respectively). Four different markers were installed along the alignment A and C close to the tensio-inclinometers. The metal box of the device $D^3_{A1}$ was also used as marker for total station measurements.

For Test 3, all the tensio-inclinometers were installed with the box at the top of the shaft turned upslope as close as possible to the ground surface to minimise overturning moments. The devices $D^3_{A1}$, $D^3_{B1}$ and $D^3_{C1}$ were placed in the soil quasi-vertically, the remaining devices were positioned following the direction orthogonal to the layer upper surface.

For test 3, the slope physical model was not tilted up to 36° as for the Test 2. It was directly tilted up to 45° to establish an overtaking angle higher than the soil friction angle and facilitate global instability of the slope.

A major instability phenomenon took place in the middle part of the slope after 16 min of rainfalls involving a soil about 25 cm thick, corresponding to the depth of the roots. The shorter time interval required to bring the slope to failure compared to Test 2 was attributed to a narrower root zone. Figure 16 shows images of the evolution of the slope over the test.

Figures 17, 18 and 19 show the evolution of rotation recorded by the tensio-inclinometer together with the surface displacements of the markers and the device $D^3_{A1}$ recorded by total station and the evolution of rotation combined with suction. Tensio-inclinometers installed at the depth of 25 cm, i.e. within the layer subjected to instability ($D^3_{A1}$, $D^3_{B3}$, $D^3_{C1}$) experienced significant pre-failure rotation clearly indicating that instability was approached. The devices installed along the alignment “A” and “C” recorded rotation values of about 30°. The devices positioned on the middle alignment of about 3°.

Two tensio-inclinometers installed along the middle alignment were affected by a malfunctioning, so only the paths recorded by the devices $D^3_{B1}$ $D^3_{B2}$ are plotted in Figure 18.

Also for the test 3, the evolution of rotations is highly consistent with the evolution parallel-to-slope displacements recorded by the motorized total station. As expected, the tensio-Inclinometers ($D^3_{B1}$, $D^3_{B2}$) installed in the zone that remained stable experienced little or no rotation.

For the tensio-inclinometers installed at shallower depths, the general pattern followed by suction and rotation is very similar to the one already described for the previous tests: rotation increases as suction decreases. A rotation increase is recorded well ahead of global instability.

## 4 DISCUSSION

The results of the tests carried out in the slope physical model clearly indicate that the volcanic silty slope experiences suction-induced deformation under the effect of a simulated rainfall. This deformation is detectable well in advance of global instability and, as a result, it can be considered a potential landslide precursor in synergy with rainfall and suction records. It should be highlighted that the inevitable effect of the lateral boundaries tends to generate arching and, hence, hinder pre-failure deformation compared to the one that would develop in open slope. In other words, boundary effects do not undermine the experimental results as far the pre-failure deformation is concerned.

The same tests also indicate that the suction-induced deformation is adequately captured by tilting evolution. Its measurement can therefore successfully replace measurements of absolute surface displacements. This finding is crucial in designing and implementing light and effective LEWS monitoring systems because measuring the rotation of a tensiometer shaft installed in the slope (with the added benefit of suction measurement) is considerably simpler than setting of displacement monitoring system which is typically expensive and difficult to install and manage (Uchimura et al., 2015). Techniques for monitoring displacements also tend to become highly inaccurate under conditions of persistent rainfalls, which are those expected when the LEWS is in operation. In contrast, the tensio-inclinometer is expected to operate trouble-free even under adverse weather conditions.

The tests have shown the good synergy between tilting and suction in detecting the state of the soil prone to landslide initiation. The Suction-Tilting (ST) for different tests are depicted in Figures 20, 21 and 22.

With reference to Test 1, the pattern towards instability may develop according to three different stages (Figure 20). The first stage is characterised by a sub-vertical trend (0-1) where drop in suction in the very shallow portion of the ground (not detected yet by the relatively deep tensiometer tip) induces soil softening that triggers tilting. In the second stage (1-2), characterized by a concave trend towards suction-axis, tilting increases driven by the downward infiltration of rainwater now sensed by the tensiometer tip. In stage (2-3), characterised by a convex trend towards the suction-axis, suction drops significantly at depth of the tensiometer tip leading to an increasing rotation rate up to instability. With reference to Test 2 (Figure 21) and Test 3 (Figure 22), the ST patterns are similar although the first sub-vertical branch tends to disappear.

The curve inflection point (point 2 in figure 20) could define the threshold used to issue the alarm. In Test 1 the inflection point occurred at about 40 minutes, well in advance of the time when sliding occurred (81 minutes). In Test 2 and 3 the inflection points occurred at times much closer to failure, 10 and 7 minutes ahead of failure respectively. It should however be noted that the failure in the slope physical model occurred in a relatively short time due to the extremely high rainfall (28 mm/h) applied to the slope. In real cases, the duration of rainfall triggering slope instability would be of the order tens of hours rather than tens of minutes. An inflection point occurring mid-time would allow issuing a warning several hours in advance.

The test in the slope physical model also provides indication about the installation of the tensio-inclinometer. The most effective procedure appeared to be that of pushing the entire shaft in the layer leaving the box in close proximity with the soil ground.

## 5 CONCLUSIONS

The accuracy of early-warning systems for rainfall-induced shallow landslides may be significantly enhanced by including the monitoring of precursor variables associated with the stress-strain state of the ground (in addition to the monitoring of more traditional meteorological variables). In this context, the paper has investigated whether wetting-induced instability occurring in a special class of soils susceptible to fail upon rainfall events, that is, high-porosity silty volcanic soils, is associated with appreciable pre-failure deformations before failure. If this is the case, the combined measurement of suction and suction-induced deformation will serve as effective precursor variable to underpin landslide early-warning systems.

The paper has first presented a tensio-inclinometer specifically developed to measure suction changes and suction-induced deformation in shallow slopes. The device was developed by mounting a MEMS accelerometer to the shaft of a conventional tensiometer. On-board electronics for data digitisation, data storage and wireless data transmission, and battery-based power supply makes the device fully wireless. The tensio-inclinometer is therefore easy to deploy and install. The standing-alone tensio-inclinometer would allow designing a very flexible and adaptive monitoring system, where a small number of fixed devices is complemented by several mobile devices that can be readily deployed as needed.

The tensio-Inclinometer was then used to monitor suction and suction-induced deformation occurring in an artificial slope subjected to an artificial rainfall. It has been shown that pre-failure deformation detected via the tilting of the tensiometer shaft is an adequate landslide precursor. If recorded in combination with suction, pre-failure deformation can provide an adequate soil-based threshold. Although the interpretation of suction–tilting curves requires further investigation via mock-up and field scale tests, the preliminary results presented in the paper provide a TRL3 proof-of-concept for early-warning thresholds built upon combined measurement of suction and suction-induced kinematics, possibly via the wireless and fully deployable tensio-inclinometer. The tensio-inclinometers used in this work were relatively short and could therefore be installed at relatively shallow depths. However, it would be relatively easy to turn longer commercial tensiometers (up to 2 m) into tensio-inclinometers. These could therefore be used to monitor slopes up to two-meter thickness, which is the typical thickness range encountered in rainfall induced landslides in silty volcanic slopes.

## ACKNOWLEDGEMENTS

This work was conducted within the framework of the PhD research project: “Development of an early warning system for rainfall induced landslides based on rain gauges and tension-inclinomter measurements” under the Programme P.O.R. – CAMPANIA FSE 2014/2020 funded by the Campania region, carried out at the PhD school of Civil Systems Engineering of the University of Naples Federico II.

## REFERENCES

Alfieri L., Salamon P., Pappenberger F., Wetterhall F., Thielen J (2012).: Operational early warning systems for water-related hazards in Europe. Environmental Science& Policy, 21, 35–49, http://dx.doi.org/10.1016/j.envsci.2012.01.008,

Balzano, B., Tarantino A., and Ridley A. (2019a). Preliminary analysis on the impacts of the rhizosphere on occurrence of rainfall-induced shallow landslides. Landslides. 16(10). 1885-1901. 10.1007/s10346-019-01197-5.

Balzano, B., Tarantino A., Nicotera M. V., Forte G., de Falco M., Santo A. (2019b).: Building physically based models for assessing rainfall-induced shallow landslide hazard at catchment scale: case study of the Sorrento Peninsula (Italy). Can. Geotech. J. 56: 1291–1303 (2019) dx.doi.org/10.1139/cgj-2017-0611

Barla, M.; Antolini, F. (2016): An integrated methodology for landslides’ early warning systems. Landslides, 13, 215–228. https://doi.org/10.1007/s10346-015-0563-8

Baum, R.L., and Godt, J.W. (2010): Early warning of rainfall-induced shallow landslides and debris flows in the USA, Landslides, 7, 259–272.

Baum, R.L., Savage, W.Z., and Godt, J.W. (2008): TRIGRS – A FORTRAN program for transient rainfall infiltration and grid-based regional slope stability analysis, vers. 2.0, U.S. Geol. Survey Open-File Rep. 424, 38.

Biansoongnern S., Plungkang B., Susuk S., (2016): Development of Low Cost Vibration Sensor Network for Early Warning System of Landslides. Energy Procedia 89, 417 – 420. https://doi.org/10.1016/j.egypro.2016.05.055

Capra L, Lugo-Hubp J, Borselli L. (2003). Mass movements in tropical volcanic terrains: the case of Teziùtlan (Mexico). Eng Geol, 69: 359–79.

Cascini L., Ferlisi S. (2003): Occurrence and consequences of flowslides: a case study, Proceedings of an International Conference on Fast Slope Movements – Prediction and Prevention for Risk Mitigation held in Napoli, 11-13 May 2003,1, 85-92, 2003

Chleborad, A. F., Baum, R. L., Godt, J. W., & Powers, P. S. (2008). A prototype system for forecasting landslides in the Seattle, Washington, area. Reviews in Engineering Geology, 20, 103-120.

Chávez J., Landaverde J., Landaverde R., and Tejnecký V. (2016). Monitoring and behavior of unsaturated volcanic pyroclastic in the Metropolitan Area of San Salvador, El Salvador. SpringerPlus. 5. 1-24. 10.1186/s40064-016-2149-x.

Chen, H., Dadson, S. and Chi Y-G (2006). Recent rainfall-induced landslides and debris flow in northern Taiwan, Geomorphology, 77 (1–2): 112-125. https://doi.org/10.1016/j.geomorph.2006.01.002.

Crosta GB, Imposimato S, Roddeman D, Chiesa S, Moia F. (2005). Small fast-moving flow-like landslides in volcanic deposits: the 2001 Las Colinas Landslide (El Salvador). Eng Geol, 79:185–214.

European Commission (2017). Horizon 2020 Work Programme 2016–2017. Available online: https://ec.europa.eu/research/participants/data/ref/h2020/other/wp/2016-2017/annexes/h2020-wp1617-annex-ga_en.pdf (accessed on 6 March 2022).

Formetta, G., Simoni, S., Godt, J.W., Lu, N., and Rigon, R. (2016): Geomorphological control on variably saturated hillslope hydrology and slope instability. Water Resour. Res., 52, 6, 4590–4607.

Fuchu D, Lee CF, Sijing W. (1999). Analysis of rainstorm-induced slide-debris flows on a natural terrain of Lantau Island, Hong Kong. Eng Geol;51:279–90.

Greco R., Pagano L. (2017).: Basic features of the predictive tools of early warning systems for water-related natural hazards: examples for shallow landslides. Natural Hazards Earth System Sciences, 17(12), 2213-2227, https://doi.org/10.5194/nhess-17-2213-2017.

Intrieri E., Gigli G., Mugnai F., Fanti R., Casagli N. (2012): Design and implementation of a landslide early warning system. Engineering Geology, 147–148, http://doi.org/10.1016/j.enggeo.2012.07.017.

Keefer D.K., Wilson R.C., Mark R.K., Brabb E.E., Brown W.M., Ellen S.D., Harp E.L., Wieczorek G.F., Alger C.S., Zatkin R.S. (1987): Real-time landslide warning during heavy rainfall, Science, 238, 921–925, http://dx.doi.org/10.1126/science.238.4829.921.

Kusumawardani, R., Kurniadhi, R., & Mukhlisin, M., Legono, D. (2017). Rainfall threshold for triggering debris flow on Merapi volcano area, Yogyakarta, Indonesia. AIP Conference Proceedings. 1818. 020027. 10.1063/1.4976891.

Mizuyama, T. and Egashira, S. (2010). Sediment Induced Disasters in the World and 1999-Debris Flow Disasters in Venezuela. Journal of Disaster Research, 5(3): 229-235.

Olivares L, Picarelli L (2003) Shallow flowslides triggered by intense rainfalls on natural slopes covered by loose unsaturated pyroclastic soils. Géotech 53(2): 283–288

Orense R.P., Towhata I., Farooq K., (2003): Investigation of failure of sandy caused by heavy rainfall. In Proceedings of the international Conference om Fast Slope Movement – Prediction and prevention for risk mitigation (FSM2003) Sorrento

Orense, R.P., Farooq, K., Towhata, I., (2004). Deformation behavior ofs andy slopes during rain water infiltration. SoilsFound.44(2),15–30. DOI:10.3208/sandf.44.2_15

Ortigao, J. A. R., Justi, M. G., d'Orsi, R., & Brito, H. (2001, December). Rio-Watch 2001: the Rio de Janeiro landslide alarm system. In Proc. 14th Southeast Asian Geotechnical Conference, edited by: Ho and Li, Hong Kong, Balkema (Vol. 3, pp. 237-241).

Pagano, L, Picarelli, L., Rianna, G., and Urciuoli, G. (2010): A simple numerical procedure for timely prediction of precipitation-induced landslides in unsaturated pyroclastic soils, Landslides, 7, 273–289.

Pecoraro G., Calvello M., Piciullo L. (2019): Monitoring strategies for local landslide early warning systems. Landslides V.16, 213–231. DOI 10.1007/s10346-018-1068-z

Picarelli L., Olivares L., Damiano E., Darban R. & Santo A. (2020). The effects of extreme precipitations on landslide hazard in the pyroclastic deposits of Campania Region: a review. Landslides volume 17, pages2343–2358 (2020)

Ponziani F., Pandolfo C., Stelluti M., Berni N., Brocca L., Moramarco T.: Assessment of rainfall thresholds and soil moisture modeling for operational hydrogeological risk prevention in the Umbria region (central Italy), Landslides, 9, 229–237, http://dx.doi.org/10.1007/s10346-011-0287-3, 2012

Reder A., Rianna G., (2021): Exploring ERA5 reanalysis potentialities for supporting landslide investigations: a test case from Campania Region (Southern Italy). Landslides, 18(5) 1909-1924.https://doi.org/10.1007/s10346-020-01610-4

Santo A., Di Crescenzo G., Del Prete S., Di Iorio L., (2012): The Ischia island flash flood of November 2009 (Italy): Phenomenon analysis and flood hazard. Physics and Chemistry of the Earth, Parts A/B/C, 49, 3-17, https://doi.org/10.1016/j.pce.2011.12.004

Perov, V., Chernomorets, S., Budarina, O. et al. (2017). Debris flow hazards for mountain regions of Russia: regional features and key events. Nat Hazards 88, 199–235. https://doi.org/10.1007/s11069-017-2841-3

Sattele M., Brundl M., Straub D., (2015): Reliability and effectiveness of early warning systems for natural hazards: Concept and application to debris flow warning. Reliability Engineering and System Safety 142, 192-202. http://dx.doi.org/10.1016/j.ress.2015.05.003

Segoni S., Rosi A., Lagomarsino D., Fanti R., Casagli N., (2018): Brief communication: Using averaged soil moisture estimates to improve the performances of a regional-scale landslide early warning system. Nat. Hazards Earth Syst. Sci., 18, 807–812. https://doi.org/10.5194/nhess-18-807-2018

Shimizu, O., Ono, M., 2016. Relationship of tephra stratigraphy and hydraulic conductivity with slide depth in rainfall-induced shallow landslides in Aso Volcano. Japan. Landslides 13 (3), 577–582.

Thiebes, B.; Bell, R.; Glade, T.; Jäger, S.; Mayer, J.; Anderson, M.; Holcombe, L. (2014): Integration of a limit-equilibrium model into a landslide early warning system. Landslides, 11, 859–875. https://doi.org/10.1007/s10346-013-0416-2

Thielicke, W. and Stamhuis, E.J., 2014. PIVlab – Towards User-friendly, Affordable and Accurate Digital Particle Image Velocimetry in MATLAB. Journal of Open Research Software, 2(1), p.e30. DOI: http://doi.org/10.5334/jors.bl

Uchimura T., Towhata I., Wang L., Nishie S., Yamaguchi H., Seko I., Qiao J., (2015): Precaution and early warning of surface failure of slopes using tilt sensors. Soils andFoundations2015;55(5):1086–1099 https://doi.org/10.1016/j.sandf.2015.09.010

UMS GmbH (last check My, the 2nd, 2021). http://library.metergroup.com/Manuals/UMS/T4_Manual.pdf

UNISDR (2006) Available at: http://www.unisdr.org/2006/ppew/info-resources/ewc3/Global-Survey-of-Early-Warning-Systems.pdf.

Yang, Z., Shao, W., Qiao, J., Huang, D., Tian, H., Lei, X., & Uchimura, T. (2017). A multi-source early warning system of MEMS based wireless monitoring for rainfall-induced landslides. Applied Sciences, 7(12), 1234.

Yamao M., Sidle R., Gomi T. and Imaizumi F. (2015). Characteristics of landslides in unwelded pyroclastic flow deposits, southern Kyushu, Japan. Natural Hazards and Earth System Sciences Discussions. 3. 6351-6378. 10.5194/nhessd-3-6351.

Zhang, S., Wang, F. & Li, R. (2022). First insight into the catastrophic Atami debris flow induced by a rain gush on 3 July 2021 in Shizuoka, Japan. Landslides 19, 527–532. https://doi.org/10.1007/s10346-021-01788-1

Zhu, H.H.; Shi, B.; Zhang, C.C. (2017): FBG-based monitoring of geohazards: Current status and trends. Sensors, 17, 452. https://doi.org/10.3390/s17030452

**FIGURE CAPTIONS**

*FIGURE 1: a) Schematic layout of the tensio-inclinometer; b) the tensio-inclinometer; c) Internal view of the metal box.*

*FIGURE 2: (a) One year data acquisition scenario. (b) Comparison between cumulated adsorbed energy consumption and batter capacity*

*FIGURE 3: Slope physical model: (a) front view; (b) lateral view in horizontal position; (c) lateral view in tilted position*

*FIGURE 4: Grain size distribution of the soil tested*

*FIGURE 5: position of nozzles, tensio-inclinometers and PIV interpreted zones for Test 1*

*FIGURE 6: Images taken at different stages of the Test 1*

*FIGURE 7: Test 1. Rotation and comparison with PIV surface displacements. (a) Devices* $D^{1}_{1}$, $D^{1}_{2}$, $D^{1}_{3}$. *(b) Device* $D^{1}_{4}$

*FIGURE 8: Test 1. Simultaneous measurement of rotation and suction. (a) Devices* $D^{1}_{1}$, $D^{1}_{2}$, $D^{1}_{3}$. *(b) Device* $D^{1}_{4}$

*FIGURE 9: Position of nozzles, tensio-inclinometers, and markers for Test 2*

*FIGURE 10: Test 2. a) Simultaneous measurement of rotation and suction. Device* $D^{2}_{C1}$*, b) failure surface*

*FIGURE 11: Images taken at different stages of Test 2*

*FIGURE 12: Test 2. a) Rotation and comparison with markers surface displacements, b) Simultaneous measurement of rotation and suction for the alignment A*

*FIGURE 13: Test 2. Simultaneous measurement of rotation and suction for the alignment B*

*FIGURE 14: Test 2. a) Rotation and comparison with markers surface displacements, b) Simultaneous measurement of rotation and suction for the alignment C*

*FIGURE 14: Test 2. a) Rotation and comparison with markers surface displacements, b) Simultaneous measurement of rotation and suction for the alignment C*

*FIGURE 15: Position of nozzles, tensio-inclinometers, and markers for the Test 3*

*FIGURE 16: Images taken at different stages of Test 3*

*FIGURE 17: Test 3. a) Rotation and comparison with markers surface displacements, b) Simultaneous measurement of rotation and suction for the alignment A*

*FIGURE 18: Test 3. a) Rotation and comparison with markers surface displacements, b) Simultaneous measurement of rotation and suction for the alignment B*

*FIGURE 19: Test 3. a) Rotation and comparison with markers surface displacements, b) Simultaneous measurement of rotation and suction for the alignment C*

*FIGURE 20 Rotation versus suction and warning threshold criterion (Test 1)*

*FIGURE 21 Rotation versus suction and warning threshold criterion (Test 2)*

*FIGURE 22 Rotation versus suction and warning threshold criterion (Test 3)*

*FIGURE S1: Graphical representation of the inclination angles returned by the MEMS accelerometer*

*FIGURE S2: Semi-conductor chip partition: main section and tensiometer section – power supply links (red); signal links (blue)*

*FIGURE S3: Data acquisition cycle for (a) data transmission mode DC and (b) data logger mode DL*

**Pre-failure suction-induced deformation to inform early warning of shallow landslides: proof of concept at slope model scale**

Coppola L. [1], Reder A.[2], Tarantino A. [3], Mannara G.[4], Pagano L.[5]

[1] Lucia Coppola, Dipartimento di Ingegneria civile, edile e ambientale, Università di Napoli Federico II, Italy (lucia.coppola@◆unina.it)

[2] Alfredo Reder, REgional Model and geo-Hydrological Impacts-REMHI, Centro Euro-Mediterraneo sui Cambiamenti Climatici, Via Thomas Alva Edison s.n.c., Caserta, 81100, Italy (alfredo.reder@cmcc.it)

[3] Alessandro Tarantino, Department of Civil and Environmental Engineering, University of Strathclyde, Scotland, UK (alessandro.tarantino@strath.ac.uk, ORCID-ID 0000-0001-6690-748X)

[4] Giovani Mannara, IVM srl - Piazza Principe Umberto I, 16 - Castellammare di Stabia, Italy (mannara@ivmtech.it)

[5] Luca Pagano, Dipartimento di Ingegneria civile, edile e ambientale, Università di Napoli Federico II, Italy (lupagano@unina.it)

CORRESPONDING AUTHOR: lucia.coppola@unina.it

KEYWORDS: shallow landslides; silty volcanic soils; soil suction; tilting; slope pre-failure deformation.

**ABSTRACT**

The majority of the Landslide Early Warning Systems (LEWS) currently in operation are based on the monitoring of rainfall data alone and this limits their performance due to false alarms generated by rainfall thresholds that are inevitably set conservative. The accuracy of LEWS may be significantly enhanced by monitoring soil-based variables associated with the stress-strain response of the ground. This paper investigates whether slope pre-failure deformation can be used as additional precursor of landslide initiation. This would lead to a substantial improvement of LEWS accuracy especially if pre-failure deformation is combined with suction monitoring. Tests were carried out using a small-scale physical model of a slope built with unsaturated volcanic silt subjected to artificial rainfall. A new device named tensio-inclinometer was purposely developed to monitor simultaneously suction and suction-induced deformation. It combines a conventional tensiometer and an accelerometer installed at the top of the tensiometer shaft. It is shown that pre-failure deformation detected by the tilting of the tensiometer shaft is an adequate landslide precursor and that, combined with suction, can provide soil-based thresholds for early warning systems.

Field Code Changed

Field Code Changed

**Formatted:** Highlight

**Formatted:** Highlight

# 1 INTRODUCTION

Rainfall-induced shallow landslides in coarse-grained volcanic fall deposits often evolve into debris flows causing significant damage and fatalities worldwide. Catastrophic events have been recorded in the last two decades in El Salvador, Hong-Kong, Indonesia, Italy, Japan, Mexico, Russia, Taiwan, and Venezuela (Fuchu et al. 1999; Cascini and Ferlisi, 2003; Olivares and Picarelli, 2003; Capra et al. 2003; Crosta et al. 2005; Chen et al 2006; Pagano et al.; 2010; Mizuyama and Egashira, 2010; Santo et al., 2012; Yamao et al 2015; Chávez et al. 2016; Shimizu and Ono, 2016; Perov et al., 2017; Kusumawardani et al. 2017; Zhang et al 2022). Volcanic soils are non-plastic and are characterised by high porosity maintained by the suction generated by the partially saturated state. The loss of suction due to rainwater infiltration in association with high porosity make this class of materials susceptible to generate fast-moving debris flows. Risk reduction strategy for this class of landslides is based on Landslide Early Warning Systems (LEWS) as the rapidity of the sliding mass movement demands alarms to be issued ahead of landslide initiation (UNISDR, 2006; Alfieri et al., 2012; Greco & Pagano, 2017). LEWS need to be informed by landslide precursors and the performance of LEWS depends directly on the precursor variables to be monitored and the model used to set alarm thresholds.

Rainfall is considered the primary and often the sole precursor variable in the majority of the LEWS currently in operation (e.g. Keefer et al., 1987; Ortigao and Justi, 2001; Chleborad et al., 2008; Baum et al., 2008; Baum & Godt, 2010; Pagano et al., 2010; Formetta et al., 2016; Pecoraro et al., 2019). The relatively low accuracy of LEWS informed solely by rainfall data leads to conservative alarm thresholds. These tend to generate repeated false alarms and induce the served communities to underreact to the warning thus undermining the effectiveness of the LEWS (Greco & Pagano, 2017; Intrieri et al., 2012; Sattele et al., 2015; Reder & Rianna, 2021). A well-performing LEWS should therefore achieve accuracy not only to avoid missed alarms but also to minimise false alarms.

To enhance the performance of LEWS the monitoring of soil volumetric water content (measured by dielectric-based sensors) has been included as additional precursor variable because the variation of volumetric water content is an indicator of loss of suction and, hence, shear strength (Orense et al., 2003; 2004; Baum et al., 2010; Ponziani et al., 2012; Thiebes et al., 2014; Uchimura et al., 2015; Segoni et al., 2018). However, volumetric water content is not a very suitable landslide precursor as pore-water pressures triggering slope failures are generally in the range of a few kilopascals either in the negative or positive range (Balzano et al., 2019 a,b). In this interval, volumetric water content is characterised by poor sensitivity in the negative range of pore-water pressures (the water retention curve tends to level off when approaching saturated conditions) and no sensitivity in the positive range of pore-water pressures. Overall, current LEWS lack of effective precursors to generate more accurate warnings.

This paper aims to investigate whether suction and suction-induced pre-failure deformation can be used as landslide precursors. Shallow slope failure in silty/sandy geomaterials typically occurs with a well-defined failure surface as detected ex post (Balzano et al., 2019 a,b). The onset of failure is characterised by relatively large displacements of the mass above the failure surface generated by very high shear deformations in proximity of the failure surface (shear band). This stage can be preceded by diffuse shear and compression plastic deformations above the failure surface and are referred to as 'pre-failure suction-induced deformations' in this work. The research question addressed in this paper is whether pre-failure deformation combined with suction monitoring can provide effective precursors of landslide initiation. This would potentially lead to substantial improvement of LEWS accuracy.

A slope physical model was used to test whether wetting-induced instability is preceded by substantial pre-failure deformations. The slope was reconstituted using natural volcanic soil reproducing similar porosity and slope inclination as encountered in the field (Balzano et al. 2019b) and then subjected to artificial rainfall until failure. Soil suction and slope deformation were monitored using a ~~Tensio~~tensio-~~Inclinometer~~ inclinometer purposely developed for this research and designed to be later deployed in the field to underpin real LEWS~~s~~. The tests presented in the paper aim to provide a TRL3 validation ('proof of concept' according to European Commission 2017) for the use of combined measurement of suction and slope deformation to anticipate the occurrence of rainfall-induced instability. Although the experiments presented in this paper focus on volcanic soils, the results are expected to be applicable to the wider class of coarse-grained silty materials.

**Formatted:** Highlight

## 2 THE TENSIO-INCLINOMETER

### *2.1 Concept*

The ~~Tensio~~tensio-~~Inclinometer~~ inclinometer was assembled by combining i) a conventional tensiometer to measure pore-water pressure in negative and positive range and ii) an accelerometer installed to the tensiometer shaft at its top to measure its inclination as a suitable proxy measurement of landslide pre-failure deformation (Figure 1).

Pore-water pressure is a more effective precursor than volumetric water content. Silty volcanic slopes are generally cohesionless and characterised by inclinations close to the friction angle. As a result, pore-water pressures triggering slope failures are generally in the range of a few kilopascals either in the negative or positive range. Tensiometers generally show accuracy to less than 1 kPa and can measure pore-water pressure in both negative and positive range. This makes pore-water pressure measured by tensiometers a better precursor of rainfall-induced shallow landsides. It should also be noted that tensiometer maintenance (re-saturation) is not required during the wet period, i.e., the period when the tensiometer data are expected to inform the LEWS. Maintenance is not therefore a disadvantage for tensiometers compared to water content dielectric-based sensor.

The measurement of tilting as proxy variable of slope deformation was favoured over measurement of surface displacements via total station, Global Positioning System (GPS), and photogrammetric techniques as implemented in other LEWS concepts (Barla & Antolini, 2016; Zhu et al., 2017). Adverse weather conditions affect the line of sight between observer and target in total station measurements, rain can weaken the GPS signal, and reduced visibility during rain events affects the quality of photographic images.

A metal box including the accelerometer and the electronics was clamped to the tensiometer shaft via a clamping hook to be easily removed for maintenance or replacement. The metal box was designed to retrofit any commercial tensiometer once the cables from the tensiometers are connected to the chip extension via the external sockets on the metal box.

The ~~Tensio~~tensio-~~Inclinometer~~ inclinometer was designed to operate wirelessly with power supplied by a battery and Wi-Fi data transmission. The electronics required for pore-water pressure and tilting measurement, data storage and data transmission are installed on a semiconductor chip. The battery and the semiconductor chip are located in the metal box secured to the tensiometer shaft (Figure 1). The device allows wireless monitoring of two precursor variables in a single element, which is an advantage with respect to approaches based on different elements connected by cables (e.g. Yang et al., 2017). The wireless design enables rapidity of installation and/or replacement and avoids malfunctioning due to cable damage by wild animals.

## *2.2 Accelerometer and tensiometer*

The tensiometer (T4, UMS GmbH, Munich, Germany) consists of an acrylic-glass shaft of variable length in-between 0.15-2 m, developed to monitor pore-water pressure in the range from - 85 kPa to 100 kPa (Figure 1). A high air-entry value saturated ceramic cup is positioned at the bottom of the shaft to allow water (under tension) to flow from the soil to the tensiometer water reservoir or vice versa. Water pressure in the tensiometer water reservoir is measured by a piezo-electric pressure sensor positioned at the top of the tensiometer water reservoir. The back of the sensing diaphragm is vented to the atmosphere via the electrical cable and, as a result, the tensiometer measures gauge pore-water pressure.

The electrical cable carrying the power supply and the output analog signal was connected to an external plug located on the metal box. The sensing diaphragm has an accuracy of better than ±0.5 kPa.

The acceleration measurement system is based on MEMS (Micro-Electro-Mechanical- Systems) capacitive accelerometer that measures the part of gravity accelerations activated by the tilting. The accelerometer returns in the three tilting components as shown in Supplementary Figure S1. An accuracy of 0.05° can be achieved for the shaft tiling angle.

## *2.3 Electronics*

### *2.3.1 Primary semiconductor chip*

An ‘all-in-one’ primary chip includes (1) MEMS accelerometer, (2) power supply, (3) power management, (4) data storage and (5) signal digitisation data wireless transmission (microcontroller) (Supplementary Figure S2).

Lithium Thionyl Chloride (Li-SOCl2) non-rechargeable batteries supply power to the system. Batteries can ensure an acquisition every ten minutes for more than one year and may be easily replaced once fully discharged. Each section is provided with a power management system, adjusting batteries voltage according to requirement of each component (2V for MEMS accelerometer and microcontroller digital circuits, 3.3 V for the analogic circuits, 5 V for the tensiometer digital circuit).

A highly performing microcontroller (codification CC1352R) is linked to all sensors and to the memory to manage all system components. It integrates a wireless transceiver, which ensures good transmission quality with the external receiver without suffering from significant electrical disturbance deriving from microcontroller activity.

A non-volatile memory (codification MX25R6435F) stores all device data. The memory capacity of 64 Mbit can ensure storage of data acquired every ten minutes for more than one year. The tensiometer extension of the semiconductor chip includes the 16 bit analog-to-digital converter (ADC). The 16-bit resolution allows pore-water pressure to be measured with resolution better than 0.01 kPa. The chip extension was designed for two tensiometer connections. In this way, two adjacent tensiometers of different length (installed in close proximity to each other to measure suction at two different depths) can be connected to a single metal box.

### *2.3.2 Extension semiconductor chip*

An extension of the semi-conductor chip including (6) power supply for the tensiometer pressure sensors and (7) analog-digital converter for the tensiometer output signal (Supplementary Figure S2). Data storage and transmission for the tensiometers was achieved via the same components installed on the primary board used for tiltmeter data.

### *2.3.3 Operating modes*

The prototype firmware and management software were developed to operate according to two different operation modes (Supplementary Figure S3):

- the data collection and real-time transmission (Wi-Fi) operation mode (DC);
- the data logger operation mode (DL) and bulk transmission on demand.

Once the data are acquired, DC mode performs a mere wireless real-time data-transfer of all digitised data, while DL mode operates the data storage followed by a wireless bulk data-transfer when requested remotely. The DC mode is activated during the rainy period when data need to be transmitted at the highest frequency to inform the early warning system. Real-time transmission is the most energy-demanding operation mode, and it is therefore only active during the wet period. The DL mode is activated during the dry period. Although tensiometer and inclinometer data are not critical in this period, it is assumed that it is still valuable acquiring pore-water pressure and deformation data. To save battery energy charge, data are acquired at lower sampling rate, stored on-board on non-volatile memory, and periodically transmitted in bulk on user demand.

The data acquisition cycle is shown in Supplementary Figure S3. At regular predetermined time intervals, the primary chip including the accelerometer and ADC and the chip extension connected to the tensiometers are switched on. The system remains on for 10 seconds to allow for tensiometer warm-up. The same time span is exploited by the ADC for self-calibration. On completion of the warm-up stage, the acquisition stage takes place. This is followed by DC data transmission or alternatively DL data storage possibly followed by a subsequent bulk data-transfer on demand. Each stage has its specific duration, optimised to save power consumption (see list in Supplementary Table S1).

Each ~~Tensio~~tensio-i~~I~~nclinometer transmits the data to a collector node over Wi-Fi (either in real-time in DC mode or in bulk on-demand in DL mode). Previous studies have indicated that Wi-Fi transmission works properly during rainfall (Biansoongnern et al., 2016). The collector node is designed to transmit the data to the remote computer via wired network in order to safeguard the robustness of transmission of the data used to inform the early-warning system. To this end, the collector node includes a USB port that allows either i) direct connection to a laptop or ii) connection to the wired network via a USB-to-Ethernet adaptor.

The management software also provides a CSV file containing diagnostic information about different components (temperature and battery level). Each metal box communicates wireless with a collector node, physically linked to a PC throughout USB interface.

#### *2.3.4 Battery duration and data storage*

To quantify duration of battery and data storage, the scenario shown in Figure 2a was considered. It consists of one month of extremely wet period with acquisition every 30 min with real-time data transmission (DC mode), 5 months of moderately wet period with data stored on-board every 3 hours (DL mode), and 6 months of dry period with data stored on-board every 6 hours (DL mode). Figure 2b compares the cumulated adsorbed energy charge in one year with the battery capacity. The battery is clearly designed in a very conservative fashion and can last several years before replacement. Data logged on-board should be downloaded at least once a year to avoid that memory full.

## 3 SLOPE PHYSICAL MODEL

The slope physical model consisted of a tilting tank with rectangular base 2 m long and 1.5 m wide (Figure 3). The height of the side walls allowed accommodating a soil layer with a maximum height of 0.5 m (in the direction orthogonal to the base). The slope physical model was designed to have the width-to-thickness ratio relatively high to minimise the effect of friction along the longitudinal boundaries. This was assumed to be a key aspect of the experimental design as lateral friction could hinder pre-failure deformation of the slope.

The side walls were built with a lower part made of steel ($h_1$ = 0.2 m) and an upper part made of Plexiglas® ($h_2$ = 0.3 m) to allow for lateral visual inspection of the slope. The downslope wall was made of a perforated steel sheet to maintain the soil layer in place once the tank was tilted and allow for water drainage at the same time. A geotextile was interposed between the base of the tank and the soil layer to increase the interface frictional resistance and promote the development of a failure surface well within the soil layer.

The tank base was supported by a steel frame with a hinge located at the tank mid-length. A hydraulic actuator operated manually allowed tilting the tank up to 45°. The tank was surmounted by three steel portals carrying each brass nozzles to generate nebulised rain. The nozzles have 1.19 mm wide orifice tips allowing water flow rates in the range between 0.32 to 1.95 l/min for water pressures between 0.2 and 10 bars respectively.

The tested soil was a non-plastic, cohesionless silty sand of volcanic origin (Figure 4). Drained isotropic-consolidated triaxial tests (not yet published) yielded a friction angle of $\phi'$=33°. Permeameter laboratory tests (not yet published) yielded a saturated hydraulic conductivity of $3\times10^{-7}$ m/s.

A high-resolution digital video camera was positioned normal to the soil layer surface to enable measurement of surface displacements via Particle-Image Velocimetry (PIV). The analysis has been performed using PIVlab, a free toolbox for MATLAB® (Thielicke and Stamhuis, 2014). The input images were divided into sub-images (interrogation areas), and for each of these, a cross-correlation was performed. The resulting correlation matrix is used to estimate the most probable displacement within each interrogation area. An interrogation area of 86 x 100 pixels (width and height respectively) has been used. It was therefore checked that the displacements did not change when the size of interrogation area was either increased to 151 x 206 pixels or decreased to 64 x 72 pixels.

**4. RESULTS**

Three tests have been carried out to explore the effect of soil bulk density and the role of vegetation. Test 1 was carried out on bare slope prepared with loose volcanic silt, 30 cm thick, and tilted to 36°. Tests 2 and 3 were carried out on slopes prepared with dense volcanic silt, 35 cm thick, vegetated with graminaceous plants, and tilted to 45°. The tank was initially positioned horizontally to form the soil layer by dry pluvial deposition and to allow vegetation to grow (tests 2 and 3). The tank was then tilted and an artificial rain of 28 mm/h was applied until global instability was observed.

**Test 1**

Average soil porosity after placement was determined by averaging the porosity of three samples taken from the layer at different locations and found equal to 67%. After deposition, the layer was moistened by rain sprinkles ~~springles~~ and covered with a waterproof sheet to allow for hydraulic equilibration for two weeks. The tank was then tilted to an angle of 36° greater than the soil friction angle.

Formatted: Highlight

It is worth noticing that the 'effective' inclination of the slope is lower than the inclination of the tank. The downslope wall imposes a constraint on the kinematics of global instability and forces the failure surface that forms parallel to the base of the tank in the upper portion of the slope to flatten mid-slope to reach the rim of the downslope wall. The 'effective' inclination of the slope (overtaking angle) is approximately given by the inclination of the segment joining the bottom of the upslope wall with the top of the downslope wall. This inclination was equal to 27.5° and actually governs the global instability.

The slope was monitored by four t~~T~~ensio-i~~I~~nclinometers. These were installed slightly leaning upslope with the heavy box at the top of the shaft turned upslope. This generated a moment that slightly compressed the soil at the contact with the upslope portion of the shaft. Devices $D^1_1$, $D^1_2$ and $D^1_3$ were installed quasi-vertically with backwards angles of 1-2°. $D^1_1$ and $D^1_3$ were pushed down to the bottom of the layer while $D^1_2$ was pushed down to the layer mid-height. Device $D^1_4$ was installed with a backward angle of 10° to explore the effect of a more eccentric top box. The positions of nozzles, t~~T~~ensio-i~~I~~nclinometers, and PIV-interpreted zones are shown in Figure 5.

Rainfall initially infiltrated into the soil layer and started to run off after ~10 min from the beginning of the artificial rainfall. After 20 min, local instability phenomena were observed involving sublayers 2-3 cm thick. The global instability was observed after 80 min and took place when suction dropped to a few kilopascals.

The rapid post-failure movement observed was likely associated with liquefaction. According to Picarelli et al. (2020), liquefaction of silty volcanic soils occurs when the mobilised stress falls within an unstable zone in the mean effective stress-deviatoric stress plane that is bounded by the critical state line and a liquefaction 'instability' line. This unstable zone widens as the soil porosity increases. For the slope in question, the 'mobilised' overtaking angle (27.5°) likely fell between the critical state friction angle (33°) and the instability line pulled down by the high soil porosity.

Figure 6 shows images of the evolution over time of the test. Figure 7 shows the rotation measured by the four devices benchmarked against the surface displacement parallel to the slope at three different locations (A to C) derived from particle image velocimetry (PIV).

The devices $D^1_1$ and $D^1_3$ show rotation that increases downslope at increasing rate until global failure is reached. The measurement of the devices $D^1_1$ and $D^1_3$ is remarkably consistent and also in fair agreement with the surface displacement in the zones A and B (Figure 7a).

The measurement of device $D^1_2$ only lasted 25 min. Over this time, its measurement was also consistent with the measurements by devices $D^1_1$ and $D^1_3$. The measurement ceased after 25 min because the device $D^1_2$ experienced instability due to the attainment of limit lateral load for the shaft. The $D^1_2$ aboveground stretch was the same as $D^1_1$ and $D^1_3$, i.e. the box at the top of the shaft generated similar torque with respect to the ground surface. However, $D^1_2$ was only inserted to the slope mid-height compared to $D^1_1$ and $D^1_3$. As a result, the pressures applied by the soil to the shaft on its downslope side were much higher to compensate for the reduced arms with respect to the ground surface. As water infiltrated into the ground and suction decreased, passive conditions were achieved and the device fell.

The device $D^1_4$ shows a progressive counter-tilting likely associated with the installation with a backward angle of 10° (Figure 7b). The portion of soil located downslope initially experienced significant surface displacement (point C in Figure 7b). The lack of support downslope to $D^1_4$ might have generated a rotational mechanism facilitating the backward rotation of the device $D^1_2$.

Figure 8 shows the simultaneous measurement of rotation and suction for the devices $D^1_1$, $D^1_2$, and $D^1_4$. A malfunctioning affected $D^1_3$, which failed in recording suction and only returned tilting evolution, and is therefore not shown in Figure 8. The device $D^1_1$ measures an initial suction of 8 kPa at the layer base. Suction progressively reduced over the test down to 2 kPa just before failure. Rotation increased consistently with suction reduction until global instability took place. It is worth noticing that the movement is recorded earlier (~20 min) than the drop in suction at ~30 min (Figure 8a). Similar observations can be made for device $D^1_2$ for the period when the shaft remained in place.

The device $D^1_4$ recorded an initial drop in suction (Figure 8b), which can partly explain the surface displacement observed at point C in Figure 7b. The rotation recorded after ~30 min, although taking place backward, also appears to be consistent with the drop in suction from 7 kPa to 2 kPa.

**Test 2**

A thicker layer (35 cm) was placed at a lower porosity and then vegetated with a grass to respectively increase the degree of particle interlocking and introduce in the layer a tightening root system.

Soil porosity after deposition was estimated by collecting three samples from the layer at different locations and measuring their porosity. It ranged between 61% and 64%. The lower porosity was expected to generate a stiffer response of the soil and, hence, probe the t~~T~~ensio-i~~I~~nclinometer to detect smaller soil deformations prior~~i~~ to failure.

The soil layer was sown with a mixture of twelve different graminaceous plants and repeatedly wetted over a month to facilitate vegetation growth. A single sowing was sufficient to cover the entire surface. Over this period roots reached the bottom of the tank. The tank was first tilted to 36°, the same inclination as Test 1. Three nozzles and six t~~T~~ensio-i~~I~~nclinometers were installed as shown in Figure 9. The tensio-inclinometers were pushed to the depths of 35, 25 ~~e~~and 10 cm (Figure 9). All the tensio-inclinometers were installed with the box at the top of the shaft turned upslope, and as close as possible to the ground surface to minimise overturning moments as observed in Test 1. The devices $D^2_{A1}$, $D^2_{B1}$ and $D^2_{C1}$ were placed in the soil quasi-vertically, the remaining devices were positioned following the direction orthogonal to the slope upper surface. The tTensio-iInclinometers were placed in the upper portion of the slope to minimise the effect of the kinematic constraint imposed by the downslope rigid wall. Instruments and markers were placed along three different lines labelled as A, B and C. Surface displacements were measured by a motorized total station targeting 4 markers placed at the top of shafts pushed into the soil layer and placed closed to the tensio-inclinometers of the alignment A and C.

In this first stage of the test, rainfall was applied long enough to generate slightly positive pore-water pressures. Figure 10a shows the evolution of tilting and suction measured by the $D^2_{C1}$ device (negative suction indicates positive pore-water pressure). The increase of rotation is highly consistent with the drop in suction.

A failure surface became visible upslope through the plexiglas wall (Fig.10b). A rotational movement occurred along the slip surface as indicated by the device counter tilting occurring at the end of the test (Figure 10a). However, the rotational movement stopped without generating a collapse mechanism. The mobilised ‘effective’ angle of 27.5° was lower than the critical state angle (33°) but also lower than the liquefaction ‘instability’ line pulled up by the lower porosity. As a result, neither liquefaction nor global instability took place.

Rainfall was then stopped, the slope was exposed to the atmosphere. Evapotranspirative fluxes acted for a week and suction increased again to about 4 kPa. The tank was then tilted up to 45°. This was aimed to raise the ‘effective’ (overtaking) inclination from 27.5° to 35°, i.e. greater than the friction angle of 33° to promote global instability of the slope.

Rainfall was applied again, with the same intensity. Rainwater initially infiltrated into the slope until some rainwater started to run-off. The presence of the diffuse root system initially inhibited local instabilities that were otherwise observed in Test 1. Global instability was observed about 70 min after the start of the rainfall. Figure 11 shows the sequence of the evolution of the slope over the test.

Figures 12, 13 and 14 show the evolution of rotation and suction recorded by the tTensio-iInclinometers together with the surface displacements of the markers recorded by total station. It is worth noticing that one of the tensio-inclinometer installed along the alignment B malfunctioned and data from this device are missing. As for Test 1, rotation increases as suction decreases. A rotation increase is recorded well ahead of global instability. However, the stiffer response of the soil ‘reinforced’ by the root system and/or the lower porosity resulted in rotations in the range 1-5° markedly lower than rotations up to 25° as recorded in Test 1 on bare soil. The evolution of rotations is highly consistent with the evolution parallel-to-slope displacements, the latter also markedly smaller than the surface displacements recorded in Test 1. Suction paths show that global instability took place under slightly positive pore-water pressures.

**Test 3**

The third test was carried out following similar deposition by pluviation as Test 2. Values of porosity after placement were consistent with those measured for Test 2. Two seeding stages were carried out to cover the entire layer surface with graminaceous plants. The first stage aimed to vegetate the central part of the surface layer whereas the second stage allowed vegetating the part of the surface layer adjacent to the walls of the tank. After about one month, the roots penetrated a relatively shallow depth (around 25 cm), i.e. roots did not reach the bottom of the tank.

The monitoring and artificial rainfall systems (Figure 15) were similar to those installed in Test 2 (Figure 9). Three different alignments considered, labelled as alignment "A", "B", and "C" respectively. The three nozzles used were the same of Test 2 and they were located along the alignment "B".

Six tensio-inclinometers were installed, distributed across the three alignments (four tensio-inclinometers were placed along the alignment "A", only one tensio-inclinometer along the remaining alignments respectively). Four different markers were installed along the alignment A and C close to the tensio-inclinometers. The metal box of the device $D^3_{A1}$ was also used as marker for total station measurements.

For Test 3, all the tensio-inclinometers were installed with the box at the top of the shaft turned upslope as close as possible to the ground surface to minimise overturning moments. The devices $D^3_{A1}$, $D^3_{B1}$ and $D^3_{C1}$ were placed in the soil quasi-vertically, the remaining devices were positioned following the direction orthogonal to the layer upper surface.

For test 3, the slope physical model was not tilted up to 36° as for the Test 2. It was directly tilted up to 45° to establish an overtaking angle higher than the soil friction angle and facilitate global instability of the slope.

A major instability phenomenon took place in the middle part of the slope after 16 min of rainfalls involving a soil about 25 cm thick, corresponding to the depth of the roots. The shorter time interval required to bring the slope to failure compared to Test 2 was attributed to a narrower root zone. Figure 16 shows images of the evolution of the slope over the test.

Figures 17, 18 and 19 show the evolution of rotation recorded by the t~~T~~ensio-i~~I~~nclinometer together with the surface displacements of the markers and the device $D^3_{A1}$ recorded by total station and the evolution of rotation combined with suction. T~~T~~ensio-inclinometers installed at the depth of 25 cm, i.e. within the layer subjected to instability ($D^3_{A1}$, $D^3_{B3}$, $D^3_{C1}$) experienced significant pre-failure rotation clearly indicating that instability was approached. The devices installed along the alignment "A" and "C" recorded rotation values of about 30°. The devices positioned on the middle alignment of about 3°.

Two tensio-inclinometers installed along the middle alignment were affected by a malfunctioning, so only the paths recorded by the devices $D^3_{B1}$ $D^3_{B2}$ are plotted in Figure 18.

Also for the test 3, the evolution of rotations is highly consistent with the evolution parallel-to-slope displacements recorded by the motorized total station. As expected, the tensio-Inclinometers ($D^3_{B1}$, $D^3_{B2}$) installed in the zone that remained stable experienced little or no rotation.

For the tensio-inclinometers installed at shallower depths, the general pattern followed by suction and rotation is very similar to the one already described for the previous tests: rotation increases as suction decreases. A rotation increase is recorded well ahead of global instability.

## 4 DISCUSSION

The results of the tests carried out in the slope physical model clearly indicate that the volcanic silty slope experiences suction-induced deformation under the effect of a simulated rainfall. This deformation is detectable well in advance of global instability and, as a result, it can be considered a potential landslide precursor in synergy with rainfall and suction records. It should be highlighted that the inevitable effect of the lateral boundaries tends to generate arching and, hence, hinder pre-failure deformation compared to the one that would develop in open slope. In other words, boundary effects do not undermine the experimental results as far the pre-failure deformation is concerned.

The same tests also indicate that the suction-induced deformation is adequately captured by tilting evolution. Its measurement can therefore successfully replace measurements of absolute surface displacements. This finding is crucial in designing and implementing light and effective LEWS monitoring systems because measuring the rotation of a tensiometer shaft installed in the slope (with the added benefit of suction measurement) is considerably simpler than setting of displacement monitoring system which is typically expensive and difficult to install and manage (Uchimura et al., 2015). Techniques for monitoring displacements also tend to become highly inaccurate under conditions of persistent rainfalls, which are those expected when the LEWS is in operation. In contrast, the tensio-inclinometer is expected to operate trouble-free even under adverse weather conditions.

The tests have shown the good synergy between tilting and suction in detecting the state of the soil prone to landslide initiation. The Suction-Tilting (ST) for different tests are depicted in Figures 20, 21 and 22.

With reference to Test 1, the pattern towards instability may develop according to three different stages (Figure 20). The first stage is characterised by a sub-vertical trend (0-1) where drop in suction in the very shallow portion of the ground (not detected yet by the relatively deep tensiometer tip) induces soil softening that triggers tilting. In the second stage (1-2), characterized by a concave trend towards suction-axis, tilting increases driven by the downward infiltration of rainwater now sensed by the tensiometer tip. In stage (2-3), characterised by a convex trend towards the suction-axis, suction drops significantly at depth of the tensiometer tip leading to an increasing rotation rate up to instability. With reference to Test 2 (Figure 21) and Test 3 (Figure 22), the ST patterns are similar although the first sub-vertical branch tends to disappear.

The curve inflection point (point 2 in figure 20) could define the threshold used to issue the alarm. In Test 1 the inflection point occurred at about 40 minutes, well in advance of the time when sliding occurred (81 minutes). In Test 2 and 3 the inflection points occurred at times much closer to failure, 10 and 7 minutes ahead of failure respectively. It should however be noted that the failure in the slope physical model occurred in a relatively short time due to the extremely high rainfall (28 mm/h) applied to the slope. In real cases, the duration of rainfall triggering slope instability would be of the order tens ~~tenths~~ of hours rather than tens ~~tenths~~ of minutes. An inflection point occurring mid-time would allow issuing a warning several hours in advance.

Formatted: Highlight

Formatted: Highlight

The test in the slope physical model also provides indication about the installation of the t~~T~~ensio-i~~I~~nclinometer. The most effective procedure appeared to be that of pushing the entire shaft in the layer leaving the box in close proximity with the soil ground.

## 5 CONCLUSIONS

The accuracy of early-warning systems for rainfall-induced shallow landslides may be significantly enhanced by including the monitoring of precursor variables associated with the stress-strain state of the ground (in addition to the monitoring of more traditional meteorological variables). In this context, the paper has investigated whether wetting-induced instability occurring in a special class of soils susceptible to fail upon rainfall events, that is, high-porosity silty volcanic soils, is associated with appreciable pre-failure deformations before failure. If this is the case, the combined measurement of suction and suction-induced deformation will serve as effective precursor variable to underpin landslide early-warning systems.

The paper has first presented a t~~T~~ensio-i~~I~~nclinometer specifically developed to measure suction changes and suction-induced deformation in shallow slopes. The device was developed by mounting a MEMS accelerometer to the shaft of a conventional tensiometer. On-board electronics for data digitisation, data storage and wireless data transmission, and battery-based power supply makes the device fully wireless. The t~~T~~ensio-i~~I~~nclinometer is therefore easy to deploy and install. The standing-alone t~~T~~ensio-i~~I~~nclinometer would allow designing a very flexible and adaptive monitoring system, where a small number of fixed devices is complemented by several mobile devices that can be readily deployed as needed.

The t~~T~~ensio-Inclinometer was then used to monitor suction and suction-induced deformation occurring in an artificial slope subjected to an artificial rainfall. It has been shown that pre-failure deformation detected via the tilting of the tensiometer shaft is an adequate landslide precursor. If recorded in combination with suction, pre-failure deformation can provide an adequate soil-based threshold. Although the interpretation of suction–tilting curves requires further investigation via mock-up and field scale tests, the preliminary results presented in the paper provide a TRL3 proof-of-concept for early-warning thresholds built upon combined measurement of suction and suction-induced kinematics, possibly via the wireless and fully deployable tTensio-iInclinometer. The tTensio-iInclinometers used in this work were relatively short and could therefore be installed at relatively shallow depths. However, it would be relatively easy to turn longer commercial tensiometers (up to 2 m) into tTensio-Iinclinometers. These could therefore be used to monitor slopes up to two-meter thickness, which is the typical thickness range encountered in rainfall induced landslides in silty volcanic slopes.

**ACKNOWLEDGEMENTS**

This work was conducted within the framework of the PhD research project: "Development of an early warning system for rainfall induced landslides based on rain gauges and tension-inclinomter measurements" under the Programme P.O.R. – CAMPANIA FSE 2014/2020 funded by the Campania region, carried out at the PhD school of Civil Systems Engineering of the University of Naples Federico II.

**REFERENCES**

Alfieri L., Salamon P., Pappenberger F., Wetterhall F., Thielen J (2012).: Operational early warning systems for water-related hazards in Europe. Environmental Science& Policy, 21, 35–49, http://dx.doi.org/10.1016/j.envsci.2012.01.008,

Field Code Changed

Balzano, B., Tarantino A., and Ridley A. (2019a). Preliminary analysis on the impacts of the rhizosphere on occurrence of rainfall-induced shallow landslides. Landslides. 16(10). 1885-1901. 10.1007/s10346-019-01197-5.

Balzano, B., Tarantino A., Nicotera M. V., Forte G., de Falco M., Santo A. (2019b).: Building physically based models for assessing rainfall-induced shallow landslide hazard at catchment scale: case study of the Sorrento Peninsula (Italy). Can. Geotech. J. 56: 1291–1303 (2019) dx.doi.org/10.1139/cgj-2017-0611

Barla, M.; Antolini, F. (2016): An integrated methodology for landslides' early warning systems. Landslides, 13, 215–228. https://doi.org/10.1007/s10346-015-0563-8

Field Code Changed

Baum, R.L., and Godt, J.W. (2010): Early warning of rainfall-induced shallow landslides and debris flows in the USA, Landslides, 7, 259–272.

Baum, R.L., Savage, W.Z., and Godt, J.W. (2008): TRIGRS – A FORTRAN program for transient rainfall infiltration and grid-based regional slope stability analysis, vers. 2.0, U.S. Geol. Survey Open-File Rep. 424, 38.

Biansoongnern S., Plungkang B., Susuk S., (2016): Development of Low Cost Vibration Sensor Network for Early Warning System of Landslides. Energy Procedia 89, 417 – 420. https://doi.org/10.1016/j.egypro.2016.05.055

Field Code Changed

Capra L, Lugo-Hubp J, Borselli L. (2003). Mass movements in tropical volcanic terrains: the case of Teziùtlan (Mexico). Eng Geol, 69: 359–79.

Cascini L., Ferlisi S. (2003): Occurrence and consequences of flowslides: a case study, Proceedings of an International Conference on Fast Slope Movements – Prediction and Prevention for Risk Mitigation held in Napoli, 11-13 May 2003,1, 85-92, 2003

Chleborad, A. F., Baum, R. L., Godt, J. W., & Powers, P. S. (2008). A prototype system for forecasting landslides in the Seattle, Washington, area. Reviews in Engineering Geology, 20, 103-120.

Chávez J., Landaverde J., Landaverde R., and Tejnecký V. (2016). Monitoring and behavior of unsaturated volcanic pyroclastic in the Metropolitan Area of San Salvador, El Salvador. SpringerPlus. 5. 1-24. 10.1186/s40064-016-2149-x.

Chen, H., Dadson, S. and Chi Y-G (2006). Recent rainfall-induced landslides and debris flow in northern Taiwan, Geomorphology, 77 (1–2): 112-125. https://doi.org/10.1016/j.geomorph.2006.01.002.

Crosta GB, Imposimato S, Roddeman D, Chiesa S, Moia F. (2005). Small fast-moving flow-like landslides in volcanic deposits: the 2001 Las Colinas Landslide (El Salvador). Eng Geol, 79:185–214.

European Commission (2017). Horizon 2020 Work Programme 2016–2017. Available online: https://ec.europa.eu/research/participants/data/ref/h2020/other/wp/2016-2017/annexes/h2020-wp1617-annex-ga_en.pdf (accessed on 6 March 2022).

Formetta, G., Simoni, S., Godt, J.W., Lu, N., and Rigon, R. (2016): Geomorphological control on variably saturated hillslope hydrology and slope instability. Water Resour. Res., 52, 6, 4590–4607.

Fuchu D, Lee CF, Sijing W. (1999). Analysis of rainstorm-induced slide-debris flows on a natural terrain of Lantau Island, Hong Kong. Eng Geol;51:279–90.

Greco R., Pagano L. (2017).: Basic features of the predictive tools of early warning systems for water-related natural hazards: examples for shallow landslides. Natural Hazards Earth System Sciences, 17(12), 2213-2227, https://doi.org/10.5194/nhess-17-2213-2017.

Intrieri E., Gigli G., Mugnai F., Fanti R., Casagli N. (2012): Design and implementation of a landslide early warning system. Engineering Geology, 147–148, http://doi.org/10.1016/j.enggeo.2012.07.017**Errore. Riferimento a collegamento ipertestuale non valido.**

Keefer D.K., Wilson R.C., Mark R.K., Brabb E.E., Brown W.M., Ellen S.D., Harp E.L., Wieczorek G.F., Alger C.S., Zatkin R.S. (1987): Real-time landslide warning during heavy rainfall, Science, 238, 921–925, http://dx.doi.org/10.1126/science.238.4829.921.

Kusumawardani, R., Kurniadhi, R., & Mukhlisin, M., Legono, D. (2017). Rainfall threshold for triggering debris flow on Merapi volcano area, Yogyakarta, Indonesia. AIP Conference Proceedings. 1818. 020027. 10.1063/1.4976891.

Mizuyama, T. and Egashira, S. (2010). Sediment Induced Disasters in the World and 1999-Debris Flow Disasters in Venezuela. Journal of Disaster Research, 5(3): 229-235.

Olivares L, Picarelli L (2003) Shallow flowslides triggered by intense rainfalls on natural slopes covered by loose unsaturated pyroclastic soils. Géotech 53(2): 283–288

Orense R.P., Towhata I., Farooq K., (2003): Investigation of failure of sandy caused by heavy rainfall. In Proceedings of the international Conference om Fast Slope Movement – Prediction and prevention for risk mitigation (FSM2003) Sorrento

Orense, R.P., Farooq, K., Towhata, I., (2004). Deformation behavior ofs andy slopes during rain water infiltration. SoilsFound.44(2),15–30. DOI:10.3208/sandf.44.2_15

Ortigao, J. A. R., Justi, M. G., d'Orsi, R., & Brito, H. (2001, December). Rio-Watch 2001: the Rio de Janeiro landslide alarm system. In Proc. 14th Southeast Asian Geotechnical Conference, edited by: Ho and Li, Hong Kong, Balkema (Vol. 3, pp. 237-241).

Pagano, L, Picarelli, L., Rianna, G., and Urciuoli, G. (2010): A simple numerical procedure for timely prediction of precipitation-induced landslides in unsaturated pyroclastic soils, Landslides, 7, 273–289.

Pecoraro G., Calvello M., Piciullo L. (2019): Monitoring strategies for local landslide early warning systems. Landslides V.16, 213–231. DOI 10.1007/s10346-018-1068-z

Picarelli L., Olivares L., Damiano E., Darban R. & Santo A. (2020). The effects of extreme precipitations on landslide hazard in the pyroclastic deposits of Campania Region: a review. Landslides volume 17, pages2343–2358 (2020)

Ponziani F., Pandolfo C., Stelluti M., Berni N., Brocca L., Moramarco T.: Assessment of rainfall thresholds and soil moisture modeling for operational hydrogeological risk prevention in the Umbria region (central Italy), Landslides, 9, 229–237, http://dx.doi.org/10.1007/s10346-011-0287-3, 2012

Reder A., Rianna G., (2021): Exploring ERA5 reanalysis potentialities for supporting landslide investigations: a test case from Campania Region (Southern Italy). Landslides, 18(5) 1909-1924.https://doi.org/10.1007/s10346-020-01610-4

Santo A., Di Crescenzo G., Del Prete S., Di Iorio L., (2012): The Ischia island flash flood of November 2009 (Italy): Phenomenon analysis and flood hazard. Physics and Chemistry of the Earth, Parts A/B/C, 49, 3-17, https://doi.org/10.1016/j.pce.2011.12.004

Perov, V., Chernomorets, S., Budarina, O. et al. (2017). Debris flow hazards for mountain regions of Russia: regional features and key events. Nat Hazards 88, 199–235. https://doi.org/10.1007/s11069-017-2841-3

Sattele M., Brundl M., Straub D., (2015): Reliability and effectiveness of early warning systems for natural hazards: Concept and application to debris flow warning. Reliability Engineering and System Safety 142, 192-202. http://dx.doi.org/10.1016/j.ress.2015.05.003

Field Code Changed

Field Code Changed

Field Code Changed

Field Code Changed

Field Code Changed

Field Code Changed

Field Code Changed

Segoni S., Rosi A., Lagomarsino D., Fanti R., Casagli N., (2018): Brief communication: Using averaged soil moisture estimates to improve the performances of a regional-scale landslide early warning system. Nat. Hazards Earth Syst. Sci., 18, 807–812. https://doi.org/10.5194/nhess-18-807-2018

Shimizu, O., Ono, M., 2016. Relationship of tephra stratigraphy and hydraulic conductivity with slide depth in rainfall-induced shallow landslides in Aso Volcano. Japan. Landslides 13 (3), 577–582.

Thiebes, B.; Bell, R.; Glade, T.; Jäger, S.; Mayer, J.; Anderson, M.; Holcombe, L. (2014): Integration of a limit-equilibrium model into a landslide early warning system. Landslides, 11, 859–875. https://doi.org/10.1007/s10346-013-0416-2

Thielicke, W. and Stamhuis, E.J., 2014. PIVlab – Towards User-friendly, Affordable and Accurate Digital Particle Image Velocimetry in MATLAB. Journal of Open Research Software, 2(1), p.e30. DOI: http://doi.org/10.5334/jors.bl

Uchimura T., Towhata I., Wang L., Nishie S., Yamaguchi H., Seko I., Qiao J., (2015): Precaution and early warning of surface failure of slopes using tilt sensors. Soils andFoundations2015;55(5):1086–1099 https://doi.org/10.1016/j.sandf.2015.09.010

UMS GmbH (last check My, the 2nd, 2021). http://library.metergroup.com/Manuals/UMS/T4_Manual.pdf

UNISDR (2006) Available at: http://www.unisdr.org/2006/ppew/info-resources/ewc3/Global-Survey-of-Early-Warning-Systems.pdf.

Yang, Z., Shao, W., Qiao, J., Huang, D., Tian, H., Lei, X., & Uchimura, T. (2017). A multi-source early warning system of MEMS based wireless monitoring for rainfall-induced landslides. Applied Sciences, 7(12), 1234.

Yamao M., Sidle R., Gomi T. and Imaizumi F. (2015). Characteristics of landslides in unwelded pyroclastic flow deposits, southern Kyushu, Japan. Natural Hazards and Earth System Sciences Discussions. 3. 6351-6378. 10.5194/nhessd-3-6351.

Zhang, S., Wang, F. & Li, R. (2022). First insight into the catastrophic Atami debris flow induced by a rain gush on 3 July 2021 in Shizuoka, Japan. Landslides 19, 527–532. https://doi.org/10.1007/s10346-021-01788-1

Zhu, H.H.; Shi, B.; Zhang, C.C. (2017): FBG-based monitoring of geohazards: Current status and trends. Sensors, 17, 452. https://doi.org/10.3390/s17030452

Field Code Changed

Field Code Changed

Field Code Changed

Field Code Changed

Field Code Changed

Field Code Changed

**FIGURE CAPTIONS**

*FIGURE 1: a) Schematic layout of the t~~T~~ensio-i~~I~~nclinometer; b) the ~~T~~tensio-i~~I~~nclinometer; c) Internal view of the metal box.*

*FIGURE 2: (a) One year data acquisition scenario. (b) Comparison between cumulated adsorbed energy consumption and batter capacity*

*FIGURE 3: Slope physical model: (a) front view; (b) lateral view in horizontal position; (c) lateral view in tilted position*

*FIGURE 4: Grain size distribution of the soil tested*

*FIGURE 5: position of nozzles, t~~T~~ensio-~~I~~inclinometers and PIV interpreted zones for Test 1*

*FIGURE 6: Images taken at different stages of the Test 1*

*FIGURE 7: Test 1. Rotation and comparison with PIV surface displacements. (a) Devices $D^1{}_1$, $D^1{}_2$, $D^1{}_3$. (b) Device $D^1{}_4$*

*FIGURE 8: Test 1. Simultaneous measurement of rotation and suction. (a) Devices $D^1{}_1$, $D^1{}_2$, $D^1{}_3$. (b) Device $D^1{}_4$*

*FIGURE 9: Position of nozzles, t~~T~~ensio-i~~I~~nclinometers, and markers for Test 2*

*FIGURE 10: Test 2. a) Simultaneous measurement of rotation and suction. Device $D^2{}_{C1}$, b) failure surface*

*FIGURE 11: Images taken at different stages of Test 2*

*FIGURE 12: Test 2. a) Rotation and comparison with markers surface displacements, b) Simultaneous measurement of rotation and suction for the alignment A*

*FIGURE 13: Test 2. Simultaneous measurement of rotation and suction for the alignment B*

*FIGURE 14: Test 2. a) Rotation and comparison with markers surface displacements, b) Simultaneous measurement of rotation and suction for the alignment C*

*FIGURE 14: Test 2. a) Rotation and comparison with markers surface displacements, b) Simultaneous measurement of rotation and suction for the alignment C*

*FIGURE 15: Position of nozzles, t~~T~~ensio-~~I~~inclinometers, and markers for the Test 3*

*FIGURE 16: Images taken at different stages of Test 3*

*FIGURE 17: Test 3. a) Rotation and comparison with markers surface displacements, b) Simultaneous measurement of rotation and suction for the alignment A*

*FIGURE 18: Test 3. a) Rotation and comparison with markers surface displacements, b) Simultaneous measurement of rotation and suction for the alignment B*

*FIGURE 19: Test 3. a) Rotation and comparison with markers surface displacements, b) Simultaneous measurement of rotation and suction for the alignment C*

*FIGURE 20 Rotation versus suction and warning threshold criterion (Test 1)*

*FIGURE 21 Rotation versus suction and warning threshold criterion (Test 2)*

*FIGURE 22 Rotation versus suction and warning threshold criterion (Test 3)*

*FIGURE S1: Graphical representation of the inclination angles returned by the MEMS accelerometer*

*FIGURE S2: Semi-conductor chip partition: main section and tensiometer section – power supply links (red); signal links (blue)*

*FIGURE S3: Data acquisition cycle for (a) data transmission mode DC and (b) data logger mode DL*

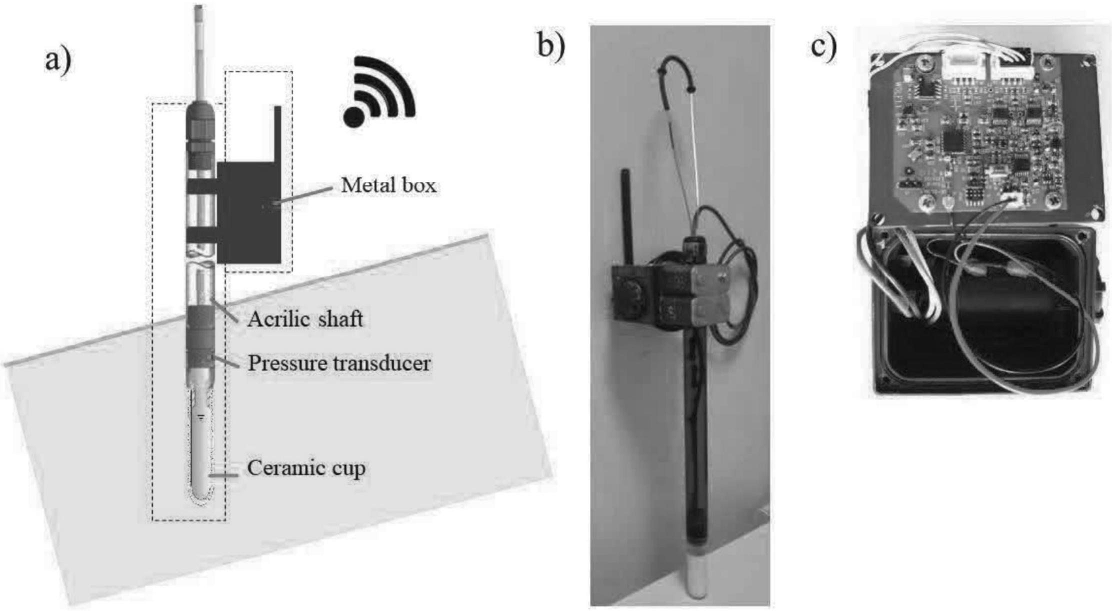


FIGURE 1: a) Schematic layout of the tensio-inclinometer; b) the tensio-inclinometer; c) Internal view of the metal box.

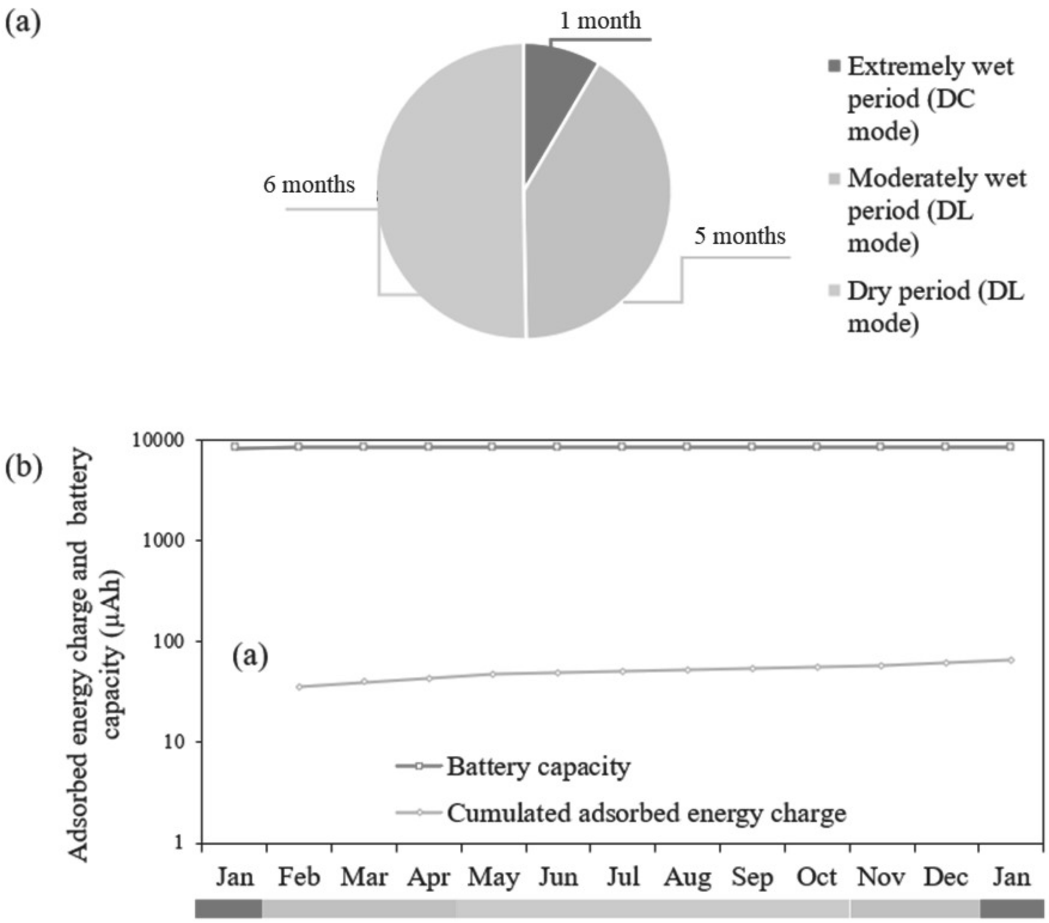


FIGURE 2: (a) One year data acquisition scenario. (b) Comparison between cumulated adsorbed energy consumption and batter capacity


FIGURE 3: Slope physical model: (a) front view; (b) lateral view in horizontal position; (c) lateral view in tilted position

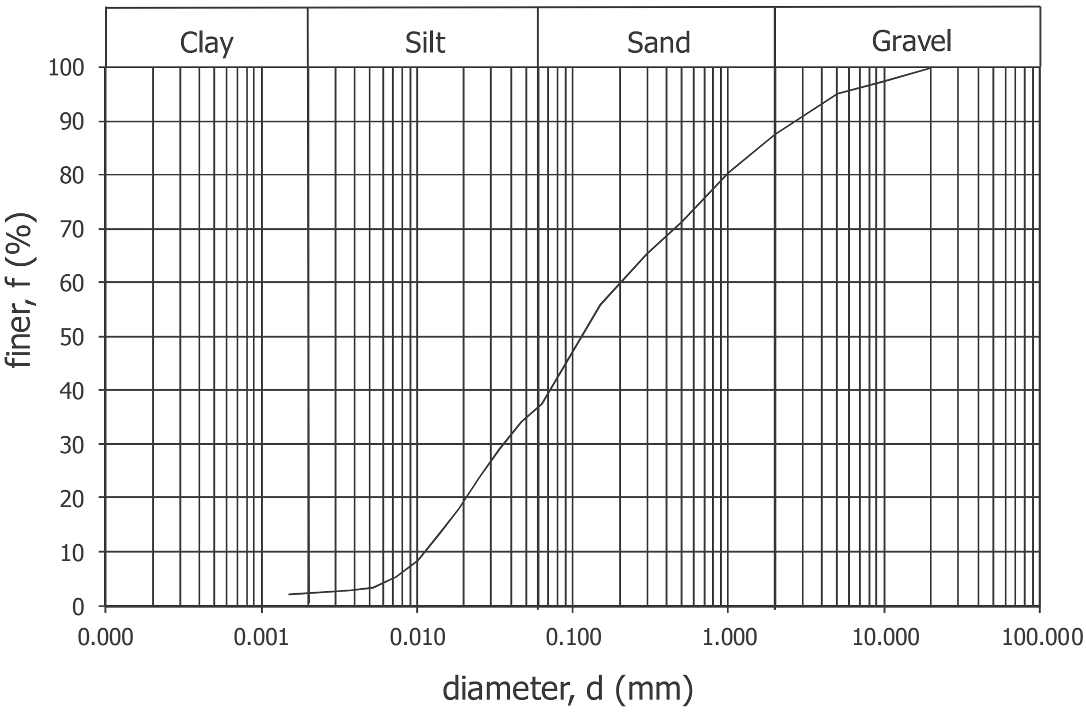


FIGURE 4: Grain size distribution of the soil tested

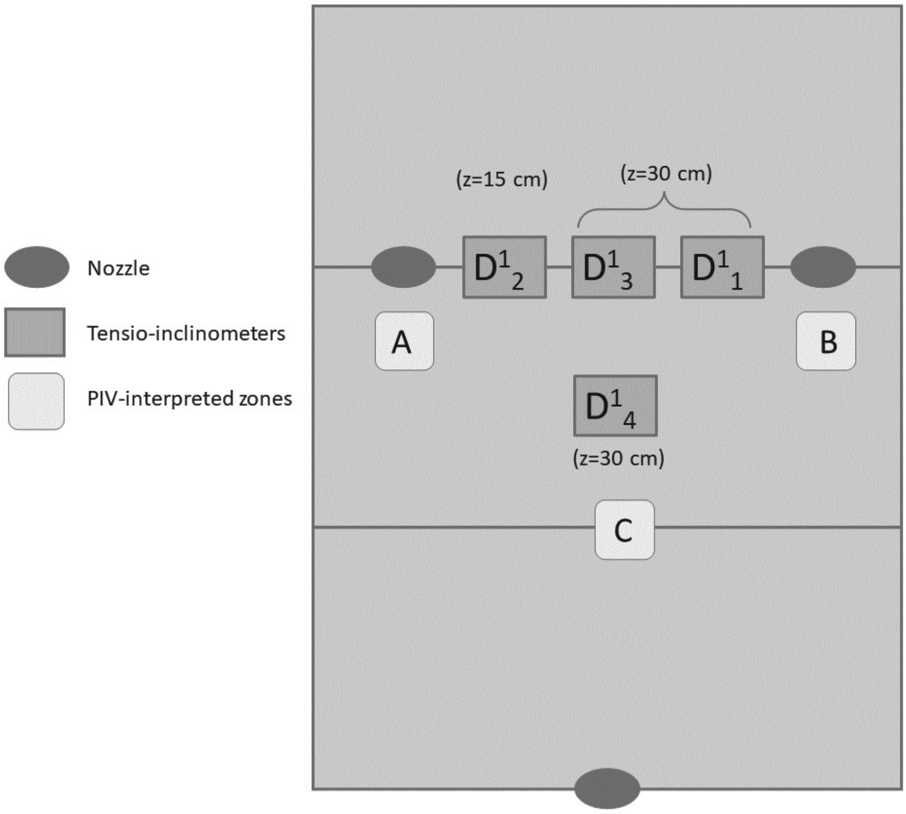


FIGURE 5: position of nozzles, tensio-inclinometers, and PIV-interpreted zones for test 1

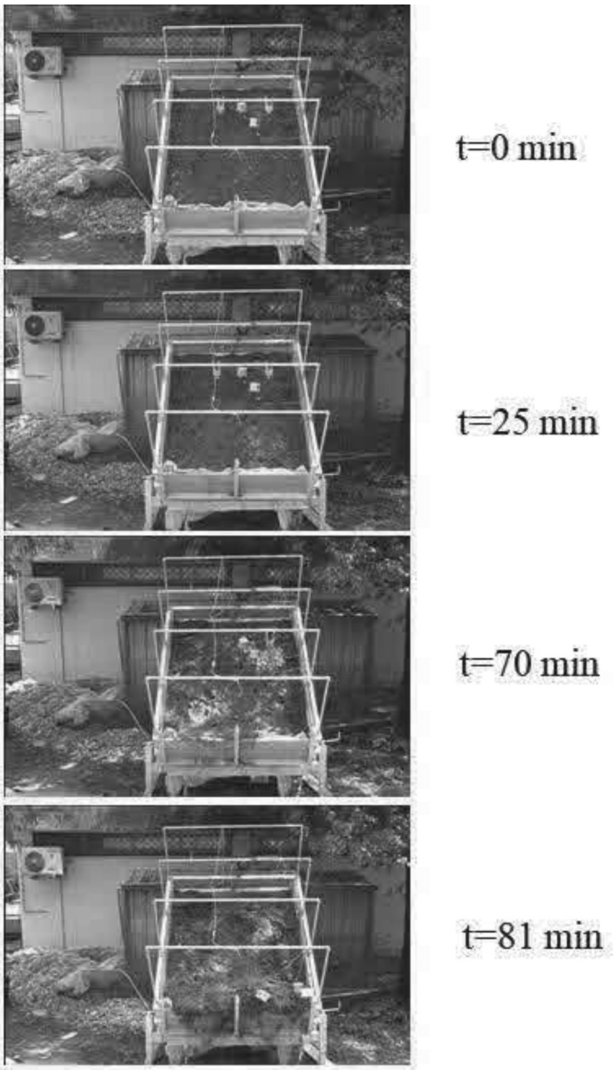


FIGURE 6: Images taken at different stages of the test 1

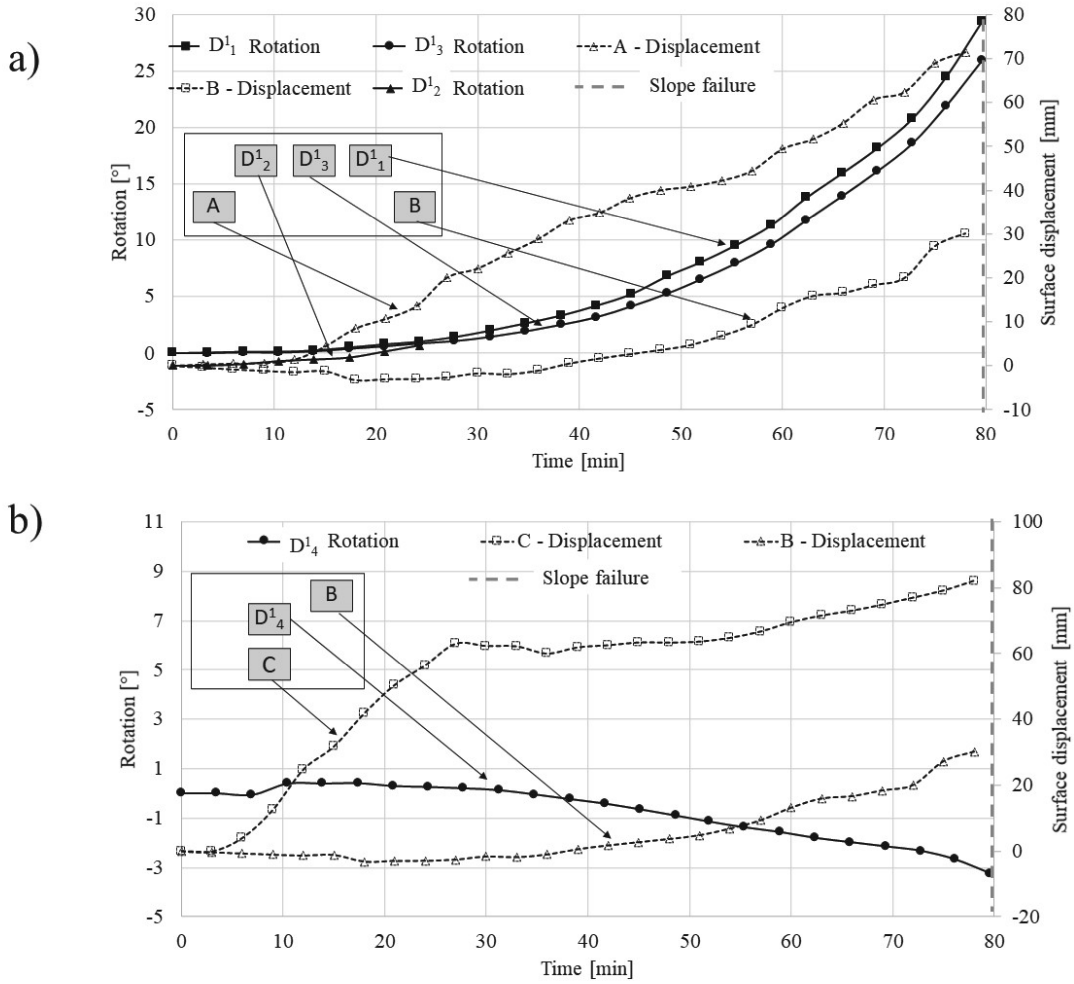


FIGURE 7: Test 1. Rotation and comparison with PIV surface displacements. (a) Devices $D^1_1$, $D^1_2$, $D^1_3$. (b) Device $D^1_4$

a)

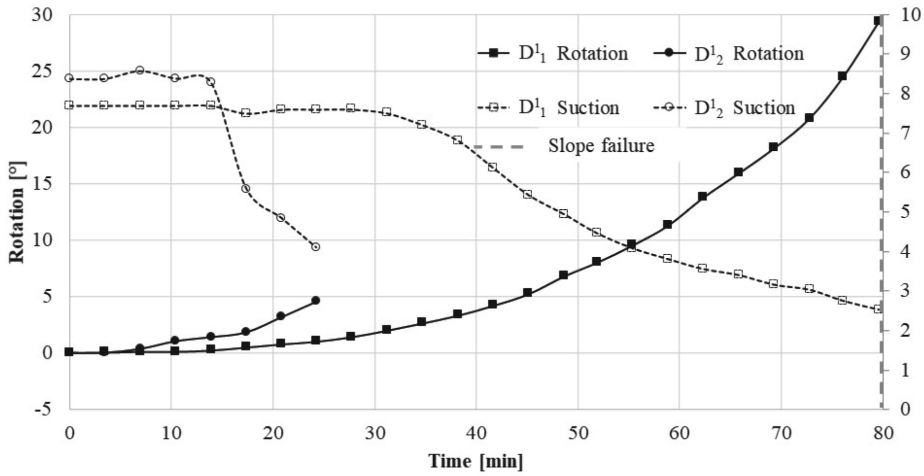


b)

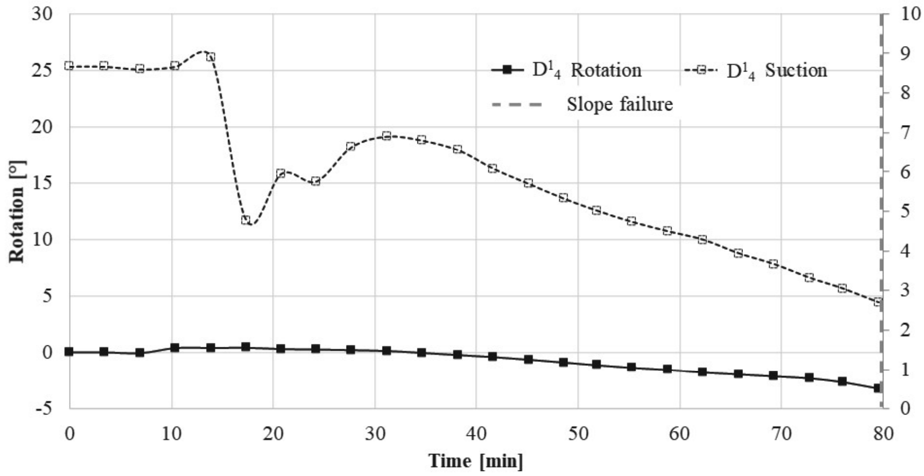


FIGURE 8: Test 1. Simultaneous measurement of rotation and suction. (a) Devices $D^1_1$, $D^1_2$, $D^1_3$. (b) Device $D^1_4$

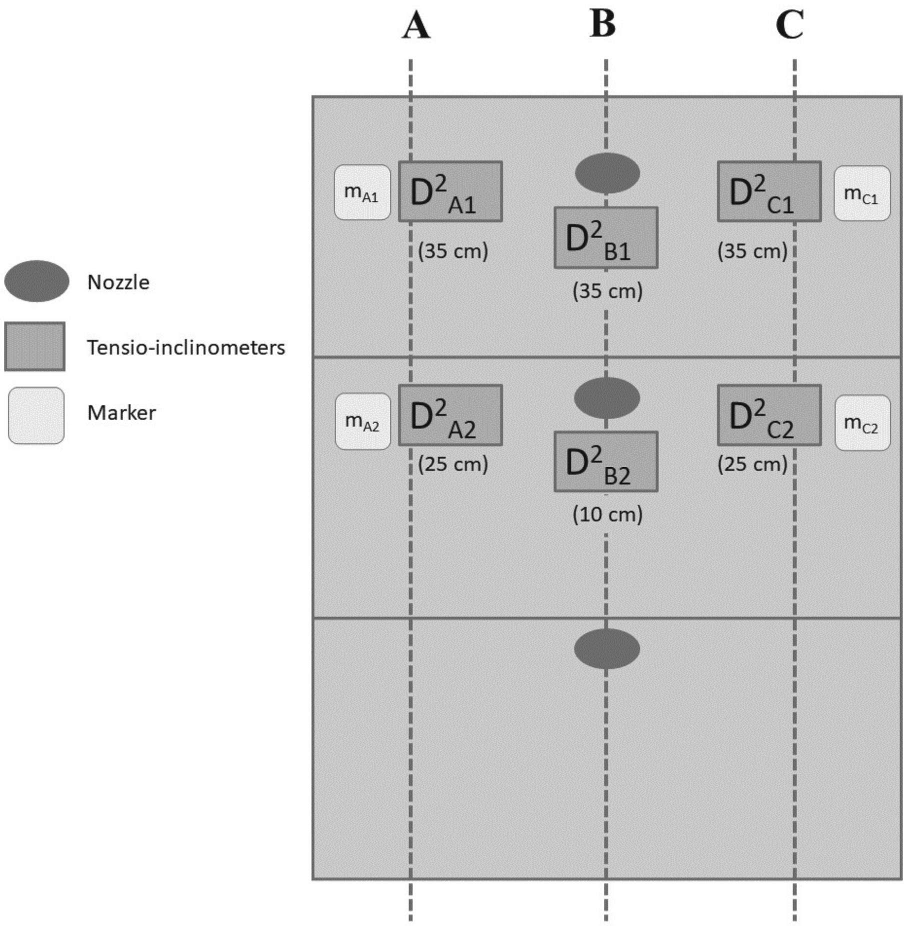


FIGURE 9: Position of nozzles, tensio-inclinometers, and markers for Test 2

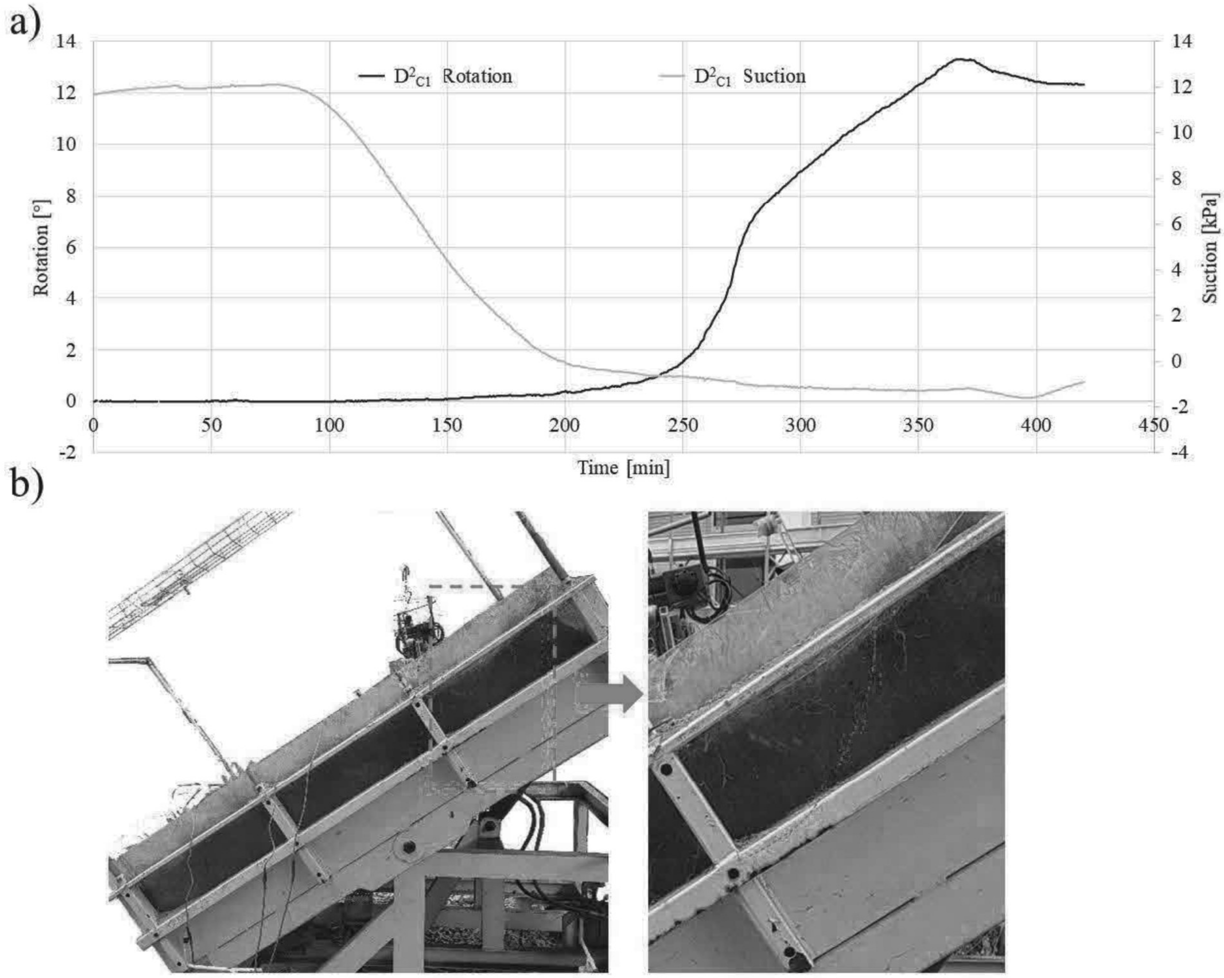


FIGURE 10: Test 2. a) Simultaneous measurement of rotation and suction. Device $D^2_{C1}$, b) failure surface

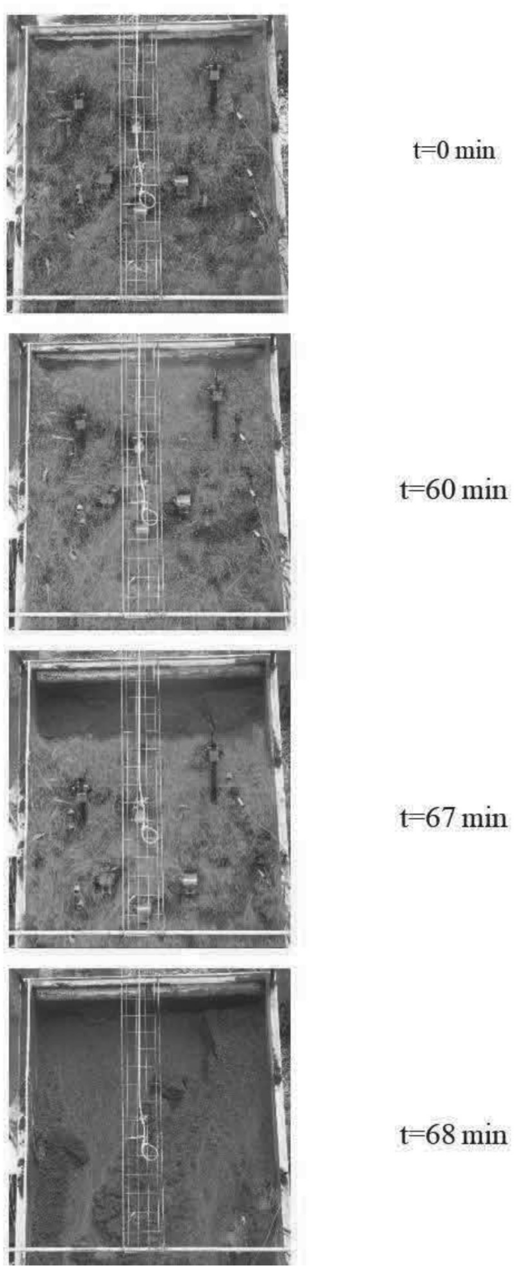


FIGURE 11: Images taken at different stages of the Test 2

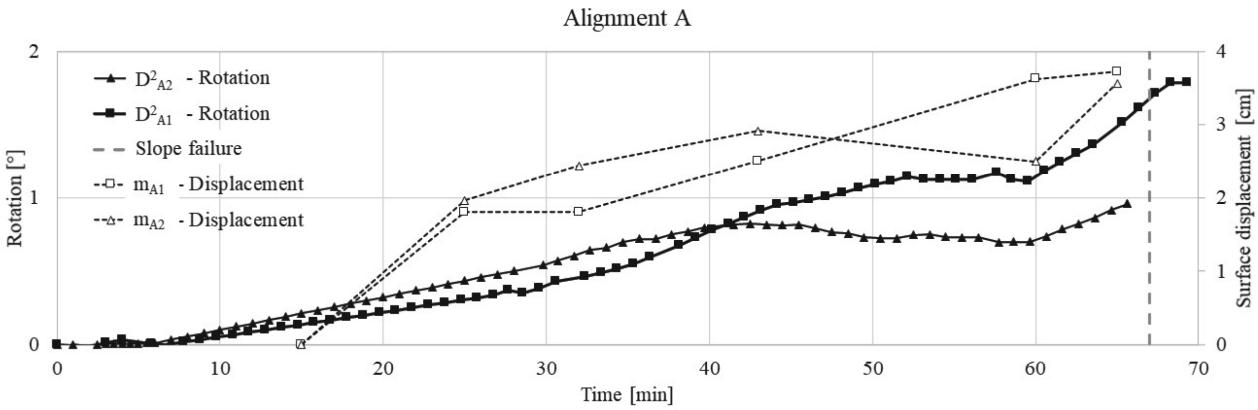


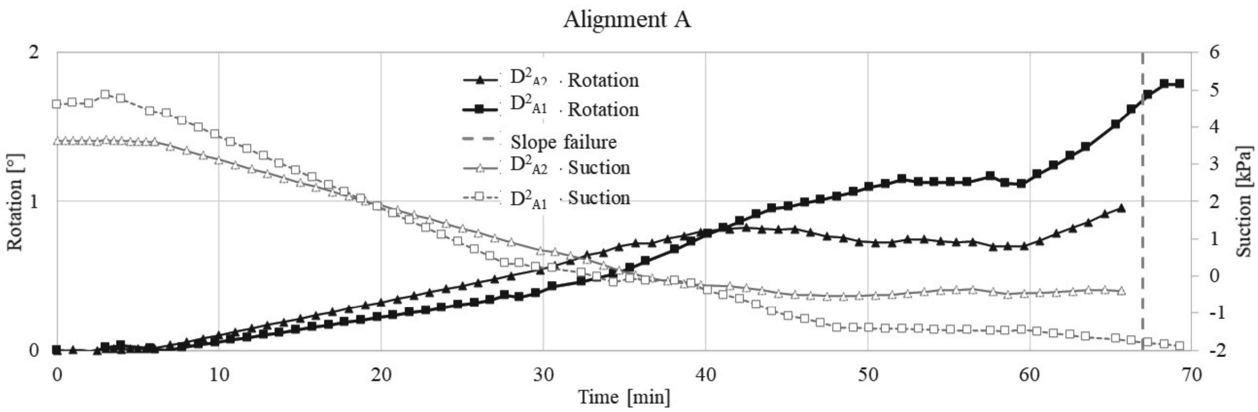


FIGURE 12: Test 2. a) Rotation and comparison with markers surface displacements, b) Simultaneous measurement of rotation and suction for the alignment A

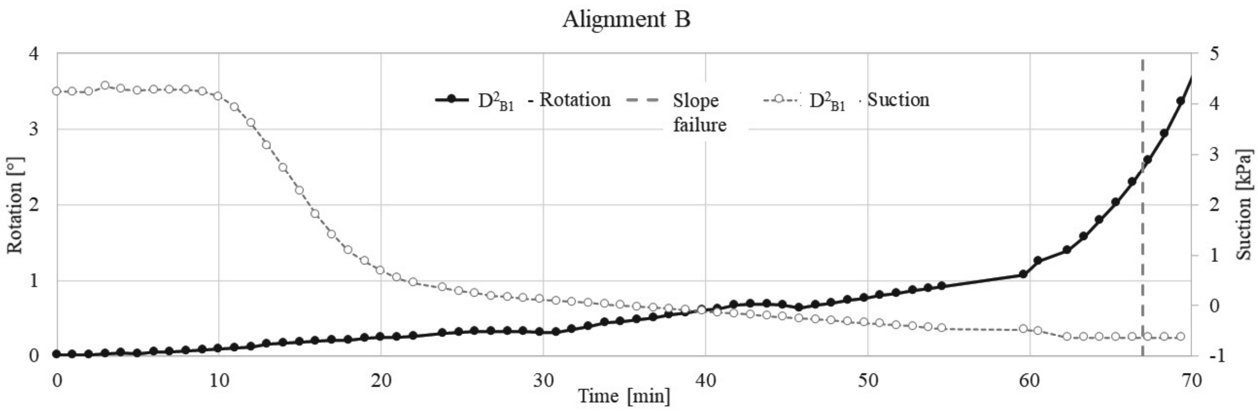


FIGURE 13: Test 2. Simultaneous measurement of rotation and suction for the alignment B

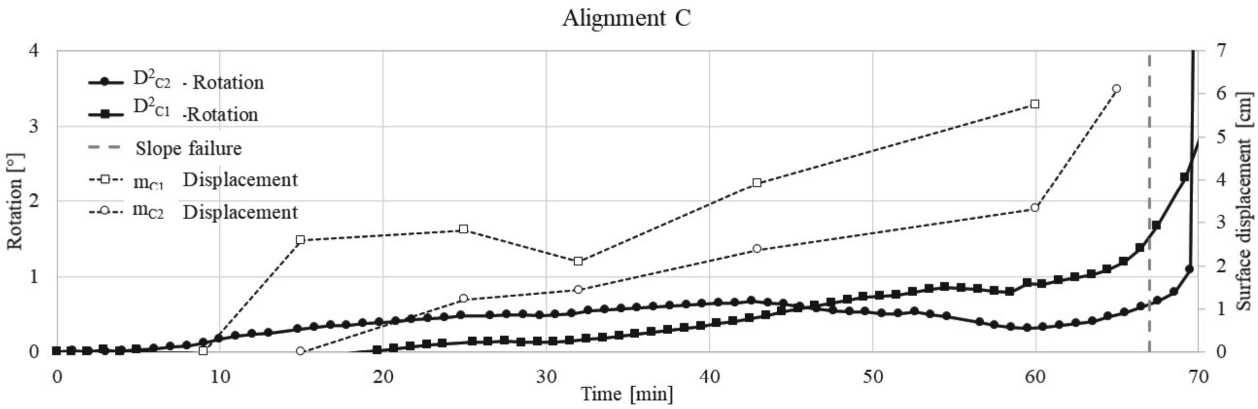


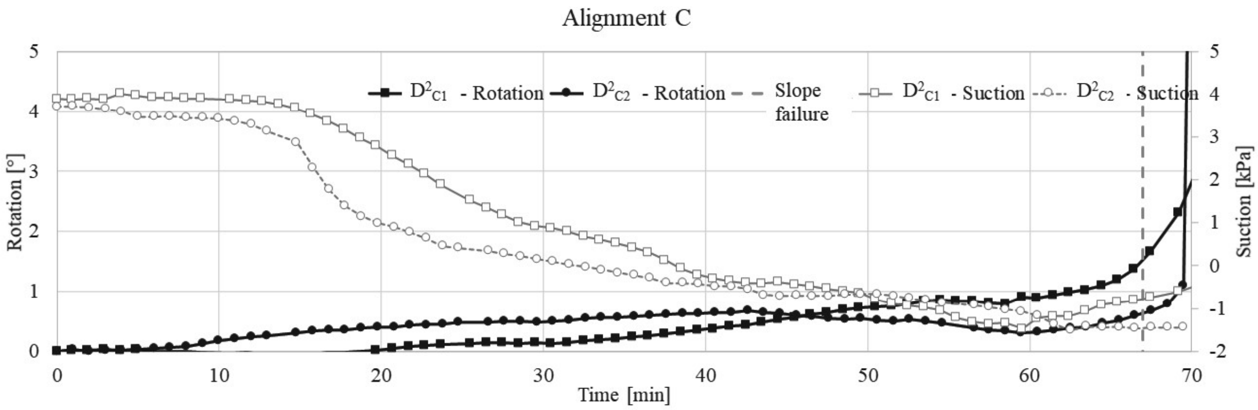


FIGURE 14: Test 2. a) Rotation and comparison with markers surface displacements, b) Simultaneous measurement of rotation and suction for the alignment C

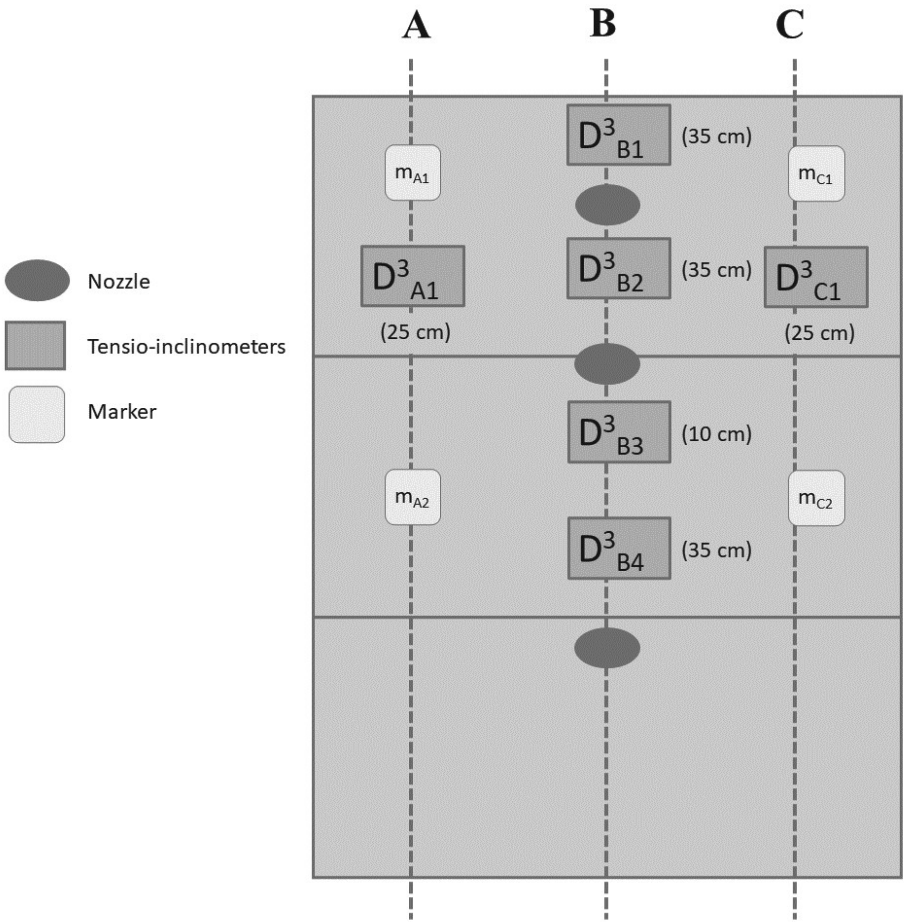


FIGURE 15: Position of nozzles, tensio-inclinometers, and markers for the Test 3

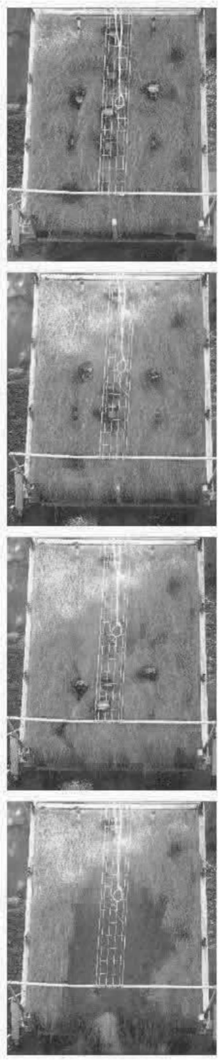

t=0 min

t=15 min

t=15 min 45 s

t=15 min 50 s

FIGURE 16: Images taken at different stages of Test 3

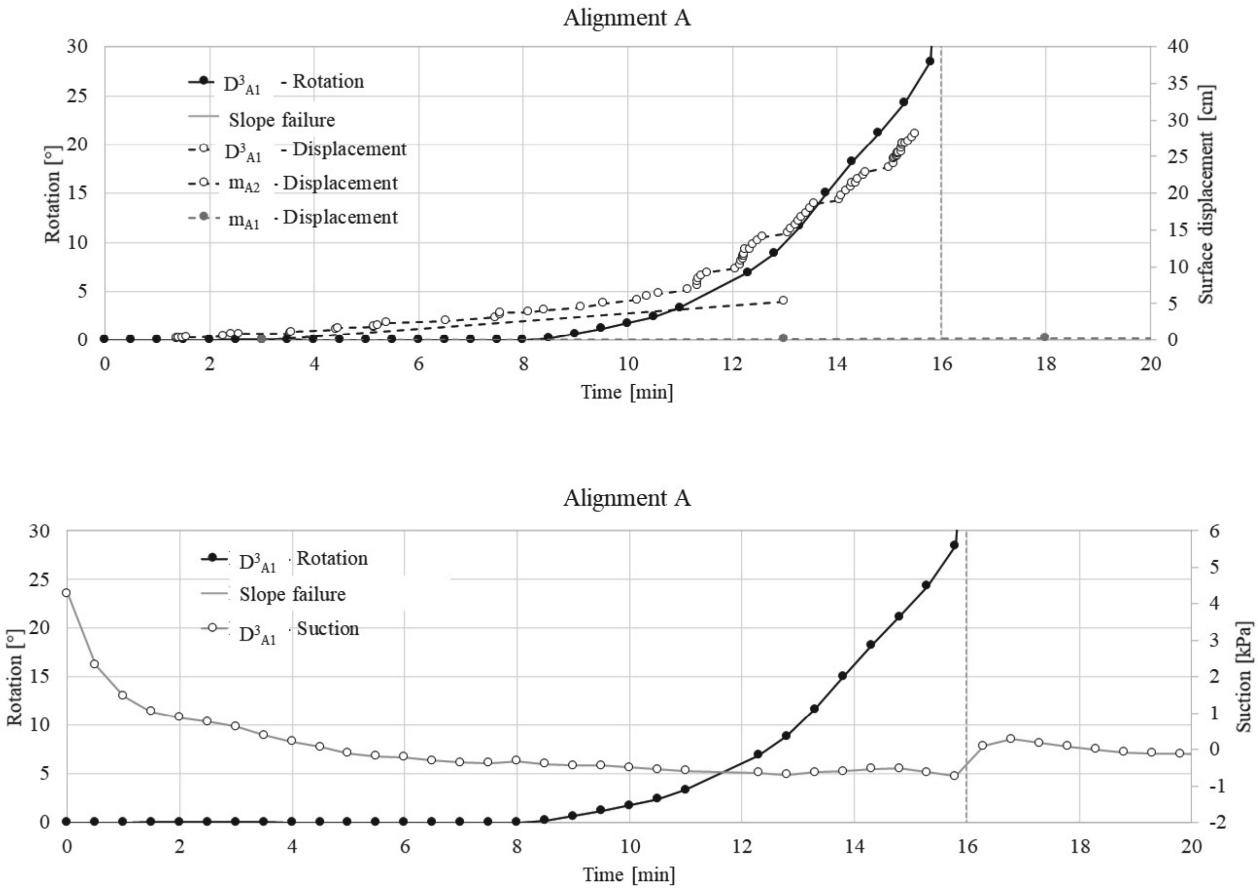


FIGURE 17: Test 3. a) Rotation and comparison with markers surface displacements, b) Simultaneous measurement of rotation and suction for the alignment A

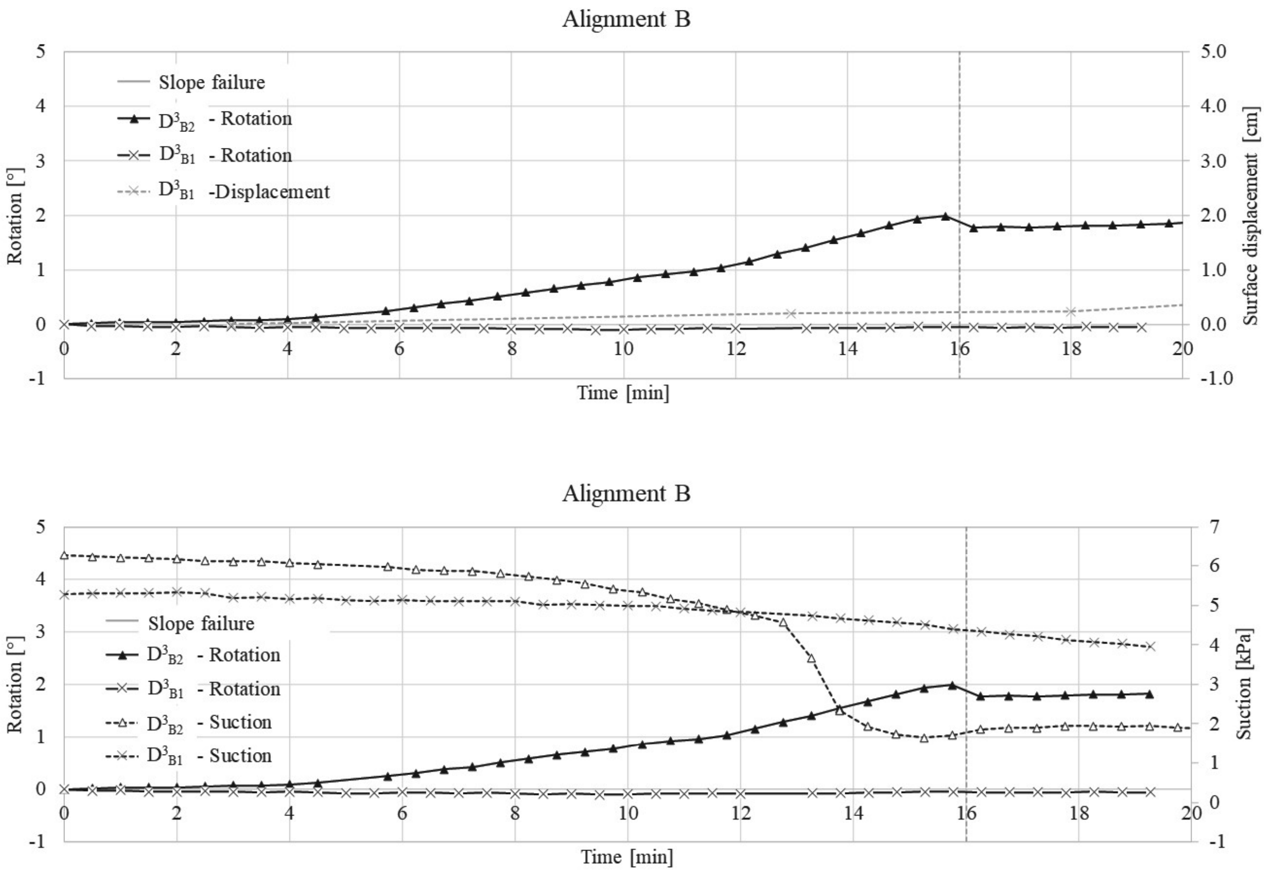


FIGURE 18: Test 3. a) Rotation and comparison with markers surface displacements, b) Simultaneous measurement of rotation and suction for the alignment B

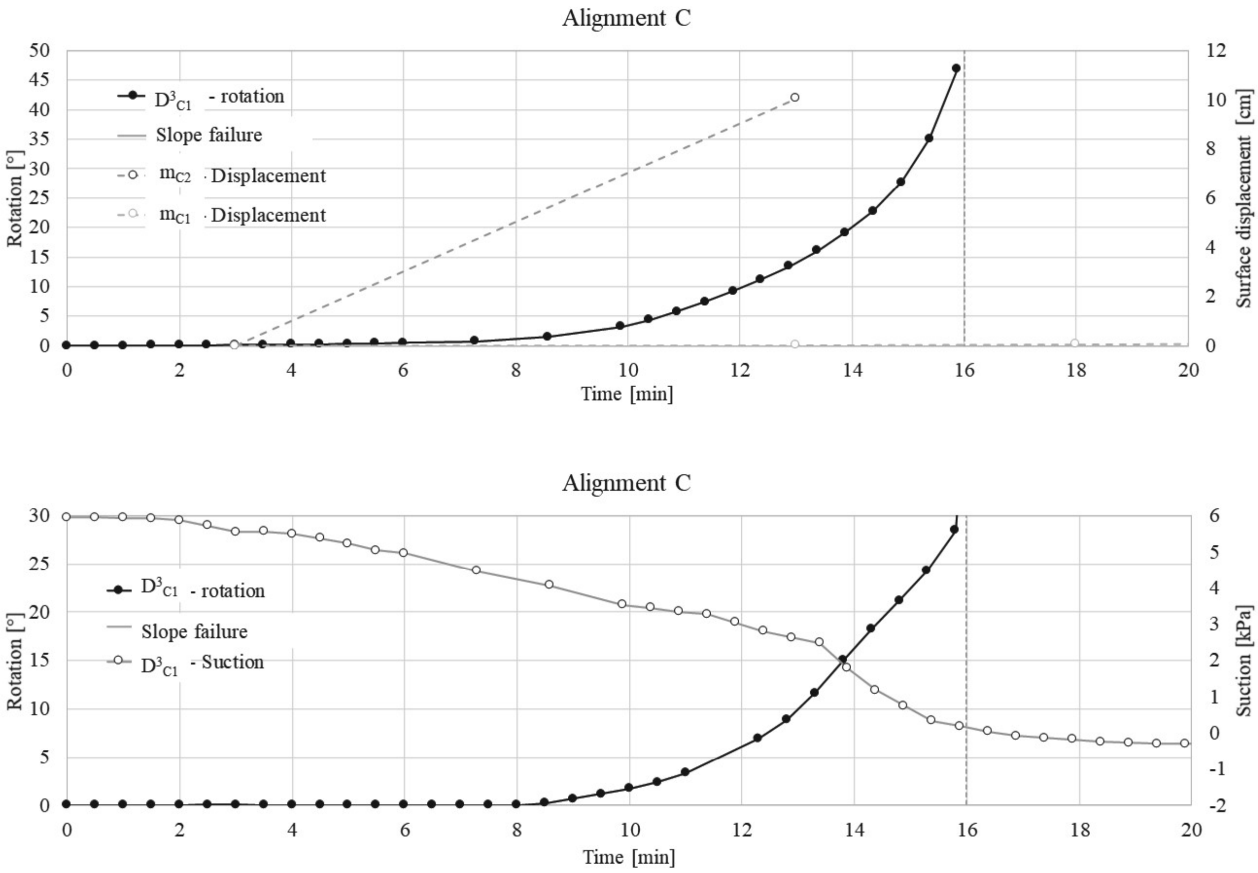


FIGURE 19: Test 3. a) Rotation and comparison with markers surface displacements, b) Simultaneous measurement of rotation and suction for the alignment C

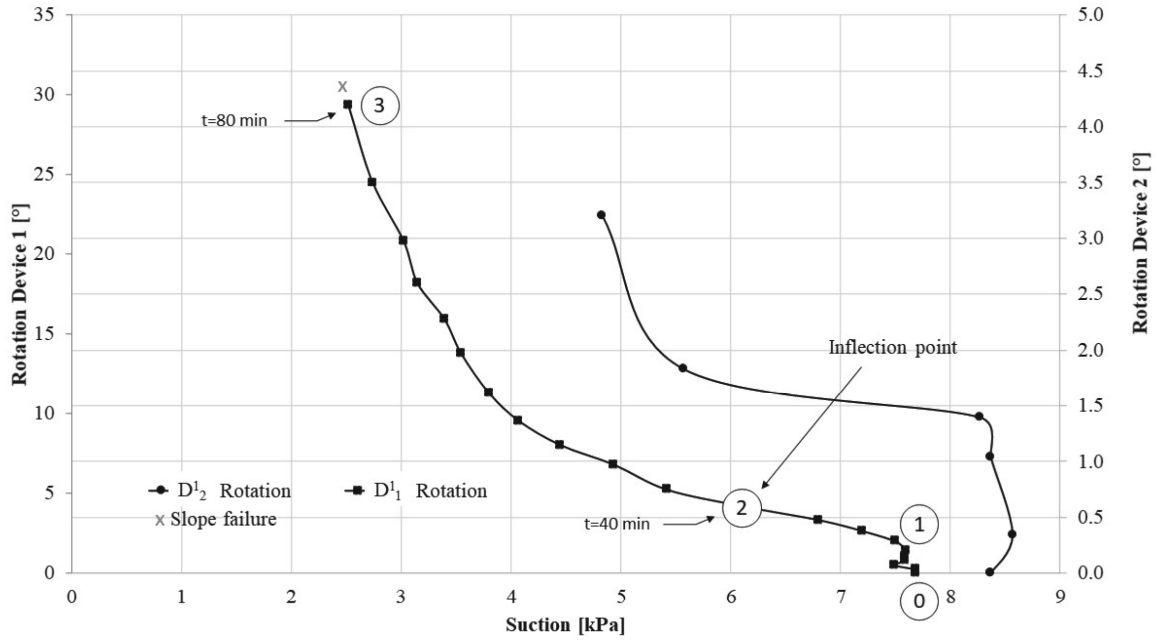


Figure 20 Rotation versus suction and warning threshold criterion (Test 1)

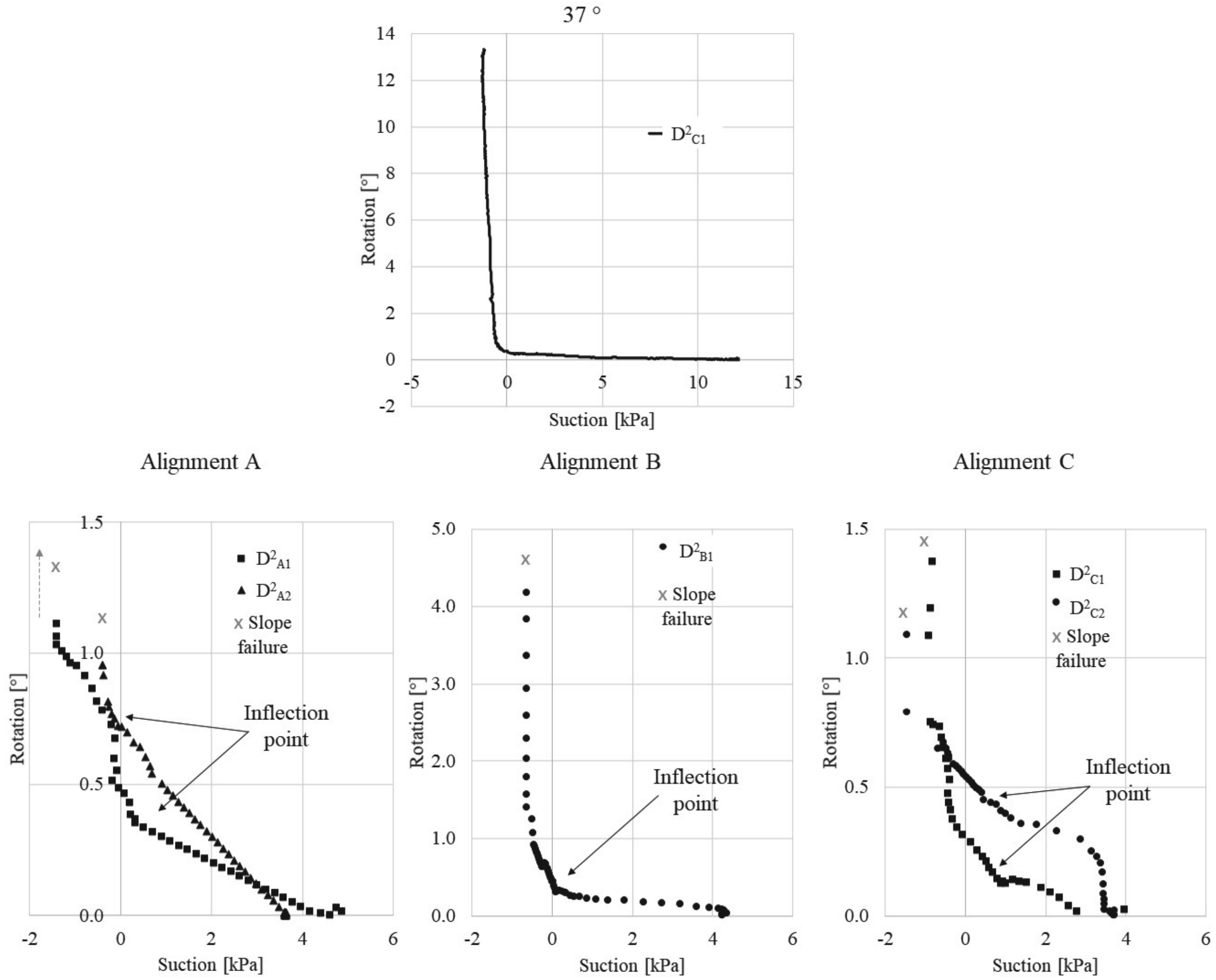


Figure 21 Rotation versus suction and warning threshold criterion (Test 2)

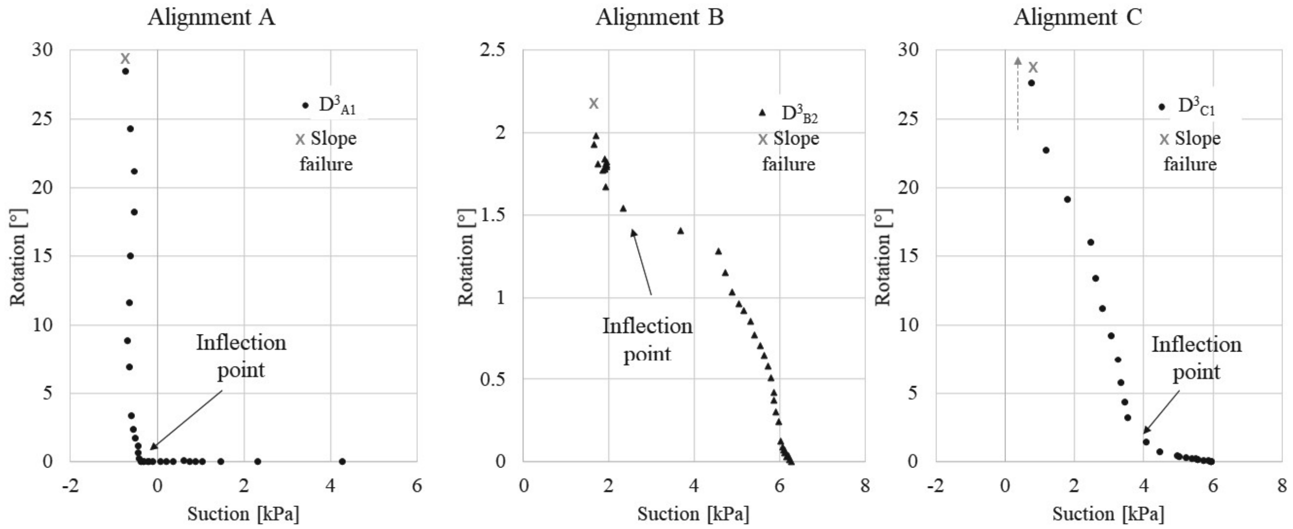


Figure 22 Rotation versus suction and warning threshold criterion (Test 3)

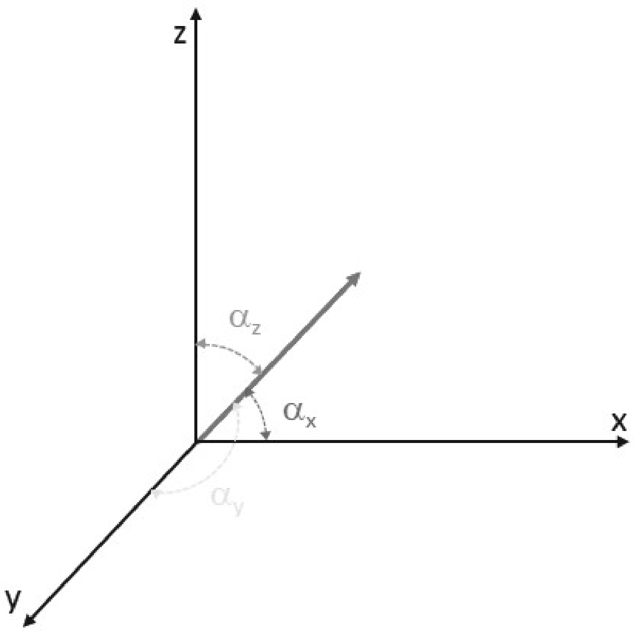


FIGURE S1: Graphical representation of the inclination angles returned by the MEMS accelerometer

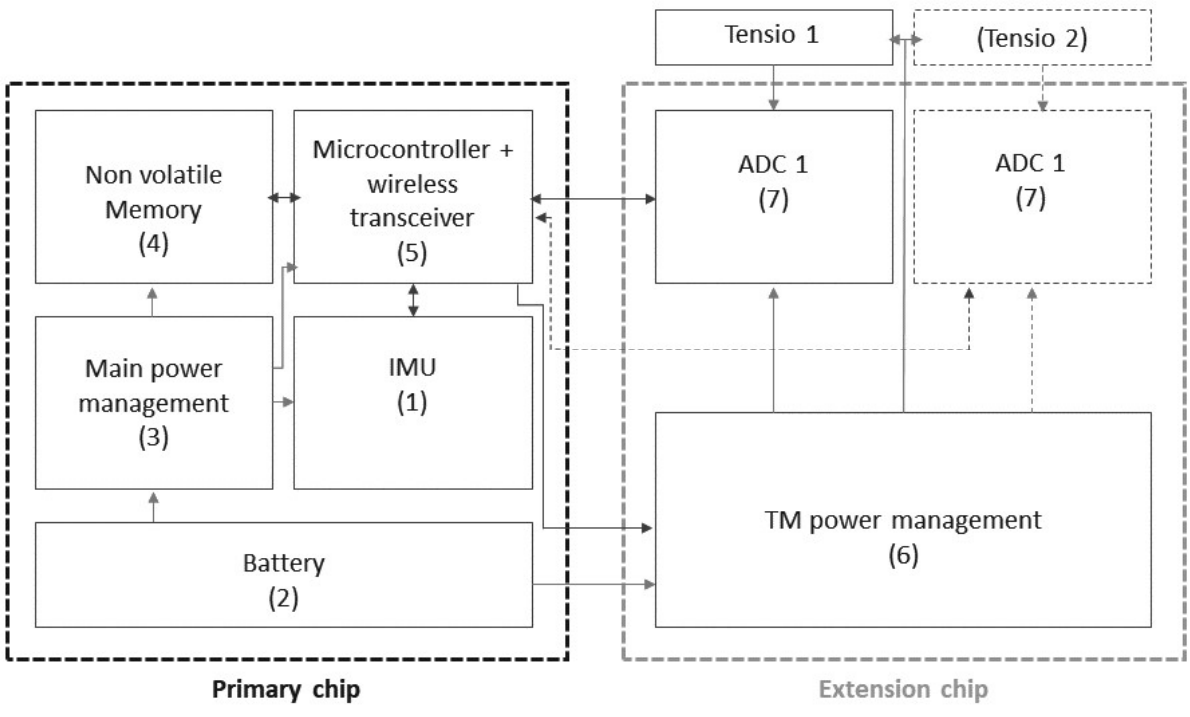


FIGURE S2: Semi-conductor chip partition: main section and tensiometer section – power supply links (red); signal links (blue)

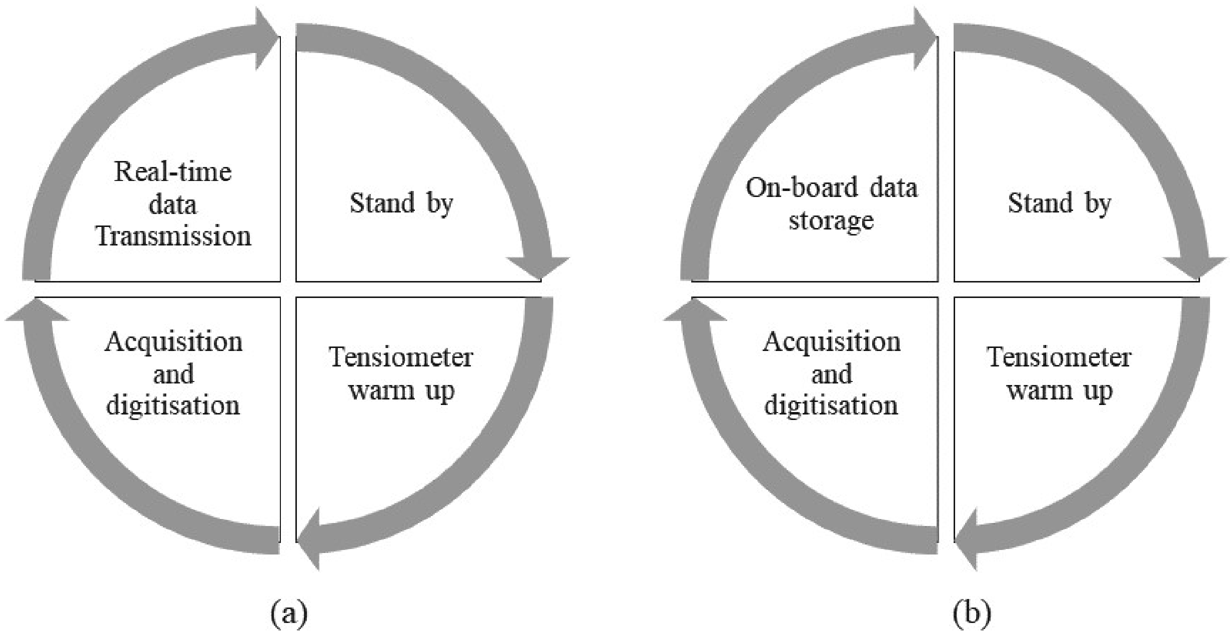


FIGURE S3: Data acquisition cycle for (a) data transmission mode DC and (b) data logger mode DL

| Step | Duration [s] | Description |
|---|---|---|
| Stand by | Variable | Every device is turned off (lowest consumption) |
| Switch on and tensiometer warm-up | 10.1 | Primary chip including accelerometer and ADC, and tensiometer chip extension are switched on for 10s for warm-up |
| Acquisition | 1.1 | Data from accelerometer and tensiometers are acquired |
| TX-RX – or Storage | 0.2 | DC mode: data are sent to the collector node;<br>DL mode: data stored in on-board memory. |
| Bulk data transmission on demand (DL mode only) | 30 | The stored data are sent to the collector node and are made available to the user if requested remotely. |

Table S1: Data acquisition cycle.

Conflict of Interest

**Declaration of interests**

☒ The authors declare that they have no known competing financial interests or personal relationships that could have appeared to influence the work reported in this paper.

☐The authors declare the following financial interests/personal relationships which may be considered as potential competing interests:

## Author Statement

Coppola Lucia and Reder Alfredo carried out the experimental tests on slope physical model.

Professors Tarantino Alessandro and Pagano Luca encouraged the work and supervised the findings of this research.

Dr. Mannara Giovanni designed the electronic sensors.

All authors discussed the results and contributed to the final manuscript.